A vegetation phenology dataset by integrating multiple sources using the Reliability Ensemble Averaging method

Yishuo Cui [1], Shouzhi Chen[1], Yufeng Gong[1], Mingwei Li[1], Zitong Jia[1], Yuyu Zhou[2], Yongshuo H. Fu[1,3]

[1]College of Water Sciences, Beijing Normal University, Beijing 100875, China
5 [2]Department of Geography, The University of Hong Kong, Hong Kong, China
[3]Plants and Ecosystems, Department of Biology, University of Antwerp, Antwerp, Belgium

Correspondence to: Yongshuo H. Fu (yfu@bnu.edu.cn), Yuyu Zhou (yuyuzhou@hku.hk)

Abstract. Global change has substantially shifted vegetation phenology, with important implications in the carbon and water cycles of terrestrial ecosystems. Various vegetation phenology datasets have been developed using remote sensing data;
10 however, the significant uncertainties in these datasets limit our understanding of ecosystem dynamics in terms of phenology. It is therefore crucial to generate a reliable large-scale vegetation phenology dataset, by fusing various existing vegetation phenology datasets, to provide comprehensive and accurate estimation of vegetation phenology with fine spatiotemporal resolution. In this study, we merged four widely used vegetation phenology datasets to generate a new dataset using the Reliability Ensemble Averaging fusion method. ~~The spatial resolution of the new dataset is 0.05° and its temporal scale spans~~
15 ~~1982–2022.~~ The new dataset has a spatial resolution of 0.05° and covers the period from 1982 to 2020, with geographic coverage extending above 30 degrees North in the Northern Hemisphere. The evaluation using a ground-based phenocam data ~~the ground-based PhenoCam dataset~~ from 280 sites indicated that the accuracy of the newly merged dataset was improved substantially. The start of growing season and the end of growing season in the newly merged dataset had the largest correlation (0.84 and 0.71, respectively with phenocam data~~respectively~~) and accuracy in terms of the root mean square error (12 and 17
20 d, respectively between phenocam data and merged datasets~~respectively~~). Using the new dataset, we found that the start of growing season exhibits a significant ($p < 0.01$) advanced trend with a rate of approximately 0.24 d yr^{-1}, and that the end of growing season exhibits a significant ($p < 0.01$) delayed trend with a rate of 0.16 d yr^{-1} over the period 1982–202~~2~~0. This dataset offers a unique and novel source of vegetation phenology data for global ecology studies.

1 Introduction

Global change has notably altered the timing of vegetation phenology (Ettinger et al., 2020; Zhang et al., 2022), leading to important implications in the carbon and water cycles of terrestrial ecosystems (Peñuelas et al., 2009; Piao et al., 2019a; Richardson et al., 2012; Zhou, 2022). Various vegetation phenology datasets using remote sensing data have been produced, but inconsistencies and uncertainties arise when comparing those datasets with ground-based phenological observations, and large variations also exist in terms of the spatiotemporal resolutions (Peng et al., 2017). Therefore, there is an urgent need to develop a highly reliable vegetation phenology product to improve our understanding of vegetation phenology dynamics, and to facilitate subsequent research on terrestrial ecosystem responses to climate change.

Ground-based phenological records were are commonly used in vegetation phenology studies (Fu et al., 2014; Geng et al., 2020; Sparks and Carey, 1995; Zhou et al., 2020). PhenoCam, as a ground-based measurement, has been operational for more than 20 years (Richardson et al., 2018a). Although ground-based observations provide high accuracy in terms of phenology dynamics, they are limited to certain locations resulting in sparse spatial coverage. In contrast, phenology datasets based on remote sensing data can cover large areas, providing comprehensive and continuous monitoring of vegetation phenology across landscapes, regions, or even continents. Additionally, remote sensing datasets are processed using standardized methods that ensure consistency and comparability across different locations and periods. However, phenology datasets based on remote sensing data do have certain limitations. Owing to differences in revisit cycles among satellites, together with sensor characteristics, sun–sensor geometry, and atmospheric conditions during imaging, substantial bias exists among the derived phenology datasets. For example, differences of >50 d in the start of growing season (SOS) have been reported among different phenology datasets based on remote sensing data (Peng et al., 2017; Zhou et al., 2020). Additionally, substantial variations in the trends of vegetation phenology exist. For example, a recent study reported that the SOS was delayed by 0.17 d yr^{-1} when based on the Global Inventory Modeling and Mapping Studies-3rd Generation (GIMMS 3g) dataset, whereas the SOS was advanced by 0.58 d yr^{-1} when based on the Moderate Resolution Imaging Spectroradiometer (MODIS) dataset in the Northern Hemisphere during 2000-2015 (Zhang et al., 2020). Previous studies found that different vegetation phenology datasets have advantages and disadvantagesmerits and demerits in different regions and over different periods (Fensholt and Proud, 2012; Zhang et al., 2020), the MODIS phenology product for the United States shows a stronger correlation with ground observations compared to the AVHRR phenology product (Peng et al., 2017), while the VIPPHEN data has fewer missing values than the MODIS phenology product. For estimates obtained using different extraction methods from the same satellite data, the discrepancies can exceed one month(White et al., 2009). Additionally, the NDVI (Normalized Difference Vegetation Index) threshold required for phenology extraction varies across different biomes (Reed et al., 1994). Because it is difficult to determine the optimal dataset from the various phenology datasets, producing a_ merged dataset using method which can choose the best dataset in different time and space among all input datasets is therefore essential for providing a comprehensive and accurate estimation of vegetation phenology with high spatiotemporal resolution.

The simple averaging method ~~was~~ is commonly employed when integrating different vegetation phenology datasets (Delbart et al., 2015; Piao et al., 2019a; Wang et al., 2019). However, the simple averaging method operates under the assumption that the reliability within each dataset is uniform, whereas it varies because of differences among the various methods of extraction (Lu et al., 2021). Alternatively, methods such as weighted functions, the Bayesian approach, and mixed models have been combined with the vegetation index method, which used the mathematical formulas to assess vegetation conditions to integrate datasets with high temporal and spatial resolutions (Walker et al., 2012; Zhu et al., 2010). Such methods can improve the data reliability of homogeneous surfaces based on the continuity of data in both time and space. Specifically, the Reliability Ensemble Averaging (REA) method, which assigns different weights to each dataset based on their reliability, has been applied to merge various datasets and consistently demonstrated high reliability through validation (Giorgi and Mearns, 2002; Lu et al., 2021; Xu et al., 2010). Therefore, the REA method has demonstrated its effectiveness in obtaining accurate merged vegetation phenology datasets.

In this study, we merged four widely used vegetation phenology datasets to generate a new dataset using the REA fusion method. The spatial resolution of the new dataset is 0.05° and its temporal scale spans 1982–~~2022~~2020. The new dataset was evaluated using data from the ground-based ~~p~~PhenoCcam dataset from 280 sites over the period 2000–2018, which provided 1410 site–year combinations. We further explored the phenological trends in spring and autumn vegetation phenology using the merged dataset. The new vegetation phenology dataset could be used in further studies on the impact of energy and carbon–water cycles within terrestrial ecosystems, together with analysis of their responses and feedbacks to global climate change (Piao et al., 2009, 2019a; Tang et al., 2016).

2 Data and Method

2.1 Phenology dataset

Four satellite-based vegetation phenology products were used to create a merged dataset, and the ground-based ~~p~~PhenocCam dataset was used for validation. The four satellite-based vegetation phenology products include (1) the MCD12Q2 (Moderate Resolution Imaging Spectroradiometer (MODIS) Land Cover Dynamics data product) phenology dataset, which was extracted from the MODIS –Land Cover Dynamics Version 6.1 derived by Friedl et al., 2022; (2) the VIP ~~dataset~~ (Making Earth System Data Records for Use in Research Environments Vegetation Index and Phenology) dataset, that was derived by Didan and Barreto, 2016, (3) the GIM_3g (GIMMS (~~NDVI3g~~Global Inventory Modeling and Mapping Studies) Normalized Difference Vegetation Index 3rd Generation) based phenology dataset, that was derived by Wang et al. (2019), and (4) the GIM_4g (~~GIMMS NDVI4g~~GIMMS(Global Inventory Modeling and Mapping Studies) Normalized Difference Vegetation Index4th Generation) based phenology dataset derived by Chen and Fu, 2024. The time span and the spatial resolution of each vegetation phenology dataset are listed in Table 1. The merged data used in this paper was clipped into

regions above 30 degrees in the Northern Hemisphere to ensure that the region was covered by four datasets. The details of each phenology dataset are introduced below.

Table 1 List of data sources

Name	Abbreviations	Sensor	Spatial Resolution	Time Span	Reference
MODIS MCD12Q2	MCD12Q2	MODIS	500m	2001-~~2022~~2020	(Friedl et al., 2022)
MEaSUREs VIPPHEN	VIP	AVHRR& MODIS	0.05°	1982-2015	(Didan and Barreto, 2016)
GIMMS NDVI3g	GIM_3g	AVHRR	1/12°	1999-2014	(Wang et al., 2019)
GIMMS NDVI4g	GIM_4g	AVHRR	1/12°	1982-2020	(Chen and Fu, 2024)

~~Note: GIM_4g refers to the phenology dataset derived the from GIMMS NDVI4g dataset, MCD12Q2 refers to the MODIS MCD12Q2 product, VIP refers to the MEaSUREs VIPPHEN dataset, and GIM_3g refers to the phenology dataset derived from the GIMMS NDVI3g dataset.~~

2.1.1 MCD12Q2 phenology dataset

The MCD12Q2 product was derived using data from the MODIS sensor onboard the Terra and Aqua satellites. The MCD12Q2 land cover dynamic product v6.1 provides a global surface phenology dataset with a 500-m spatial resolution for the period 2001–~~2021~~2020. The vegetation phenology data were extracted from the Nadir Bidirectional Adjusted Reflectance 2-band Enhanced Vegetation Index (EVI2) using the threshold method (Gray et al., 2019). The threshold method defines the growing state of the vegetation as the time when the vegetation index reaches a certain percentage of the annual amplitude and reflect a specific vegetation physiological growth stage. The MCD12Q2 phenology dataset includes greenup and dormancy (equivalent to SOS and EOS in this study, respectively). Greenup (dormancy) is defined as the date when the EVI2 time series first (last) crosses 15% of the segment EVI2 amplitude (Gray et al., 2019). The time series data was fitted by a penalized cubic smoothing spline. The amplitude is calculated as the difference between the maximum and minimum values of the EVI2 time series within the growing season. This dataset can be found at https://lpdaac.usgs.gov/products/mcd12q2v061/ (Friedl et al., 2022).

2.1.2 VIP phenology dataset

The VIP phenology dataset (VIP) was generated using data from the NASA Making Earth System Data Records for Use in Research Environments (MEaSUREs) and the Advanced Very High-Resolution Radiometer (AVHRR) over the period 1981–1999, together with MODIS/Terra MOD09 surface reflectance data over the period 2000–2014 (Didan et al., 2018). The VIP dataset includes the SOS and EOS, which were also extracted using the threshold method. The filtering method based on confidence interval and operational continuity algorithm were used to rebuild the time series curves. The start (end) of season is defined using the modified Half-Max method (White et al., 2009) as the date when the NDVI2 time series first (last) crosses

35% of the segment NDVI2 amplitude. This dataset is organized in a geographic gridded format with a spatial resolution of 0.05°. This dataset can be found at https://lpdaac.usgs.gov/products/vipphen_ndviv004/ (Didan and Barreto, 2016).

2.1.3 GIM_3g phenology dataset

The GIMMS NDVI (–Normalized Difference Vegetation Index) 3g-based phenology dataset (GIM_3g) has a spatial
115 resolution of 1/12° and covers the period 19981999–2014 (Wang et al., 2019). A double logistic function was applied to fit the NDVI curve and the threshold method was used to extract phenological dates, including the SOS and EOS. This product provides phenology data for the Northern Hemisphere, and it uses the date when the NDVI first (last) crosses 20% of the segment NDVI amplitude as the SOS (EOS). The amplitude is calculated as the difference between the maximum and minimum values of the NDVI time series within that specific segment of the growing season. This dataset can be accessed at
120 http://data.globalecology.unh.edu/data/GIMMS_NDVI3g_Phenology/ (Wang et al., 2019).

2.1.4 GIM_4g phenology dataset

The GIM_4g dataset, based on the GIMMS NDVI 4g dataset acquired by the AVHRR sensors, has a spatial resolution of 1/12° and a temporal scale spanning 1982–2020. Two steps were adopted in the process to extract phenological dates. First, the NDVI time series data were fitted and smoothed using five fitting methods: the HANTS-Maximum, Spline-Midpoint,
125 Gaussian-Midpoint, Timesat-SG, and Polyfit-Maximum methods. Second, the threshold method was used to extract phenological dates, using the date when the NDVI first (last) crosses 20% (50%) of the segment NDVI amplitude as the SOS (EOS) (Chen et al., 2024; Chen and Fu, 2024). The amplitude is calculated as the difference between the maximum and minimum values of the NDVI time series within that specific segment of the growing season. The average spring (SOS) and autumn (EOS) phenological dates were produced from the results of the five fitting methods. The GIM_4g phenology dataset
130 is available at https://doi.org/10.5281/zenodo.11136967 (Chen and Fu, 2024).

2.1.5 Camera-based phenology dataset

The A ground-based pPhenoCcam dataset, with phenological dates extracted from camera-derived images with high spatial resolution and reliable accuracy, was used to validate the merged dataset. The pPhenocCam dataset comprises three datasets. The first dataset, i.e., the PhenoCam Dataset v-2.0 (Richardson et al., 2018b; Seyednasrollah et al., 2019a, b), includes
135 data acquired derived fromusing conventional visible-wavelength automated digital camera imagerya downward facing automatic digital fisheye camera system through PhenoCam Network (Richardson et al., 2018a) over the period 2000–2018 and across 393 sites in various ecosystems, for detailed information, please refer to https://daac.ornl.gov/VEGETATION/guides/PhenoCam_V2.html and https://phenocam.nau.edu/webcam/ . It, comprisesing deciduous broadleaf, deciduous needleleaf, evergreen broadleaf, evergreen needleleaf, grassland, mixed vegetation, shrubland,
140 tundra, and wetland ecosystems, mainly in regions of Europe and North America (https://daac.ornl.gov/) (Moon et al., 2021; Ruan et al., 2023). Spline interpolation method was applied to PhenoCam data to extract transition dates for each ROI mask

in PhenoCam Dataset v2.0. We used the date when the GCC first (last) crosses 25% of the GCC amplitude as the SOS and EOS.

The second PhenoCam dataset is from the Japan Internet Nature Information System digital camera data (http://www.sizenken.biodic.go.jp/) acquired over the period 2002–2009. Ide and Oguma (Ide and Oguma, 2010) provided greenup dates for two phenocam sites with areas of interest (AOI) defined at the species level scale. The vegetation types included in their data comprise deciduous broadleaf forest, wetland, and mixed deciduous forest. The date of green-up each year was estimated as the DOY of the maximum rate of increasing 2G-RBi (i.e., the maximum of the second derivative.

The third dataset consists of phenology data for deciduous broadleaf forests in Japan (Inoue et al., 2014) supported by the Phenological Eyes Network (http://www.pheno-eye.org/), which is a network of ground-based observatories for long-term automatic observation of vegetation dynamics established in 2003 (Nasahara and Nagai, 2015), the start and end of season is defined as the first day when 20% of leaves had flushed and the first day when 80% of leaves had fallen in the given ROI, respectively. For use in this study, we deleted 26 sites which only have one direction of transition dates, and removed 90 sites with no phenology values in four data sources, then selected PhenoCam data from 280 sites over the period 2000–2018, which provided 1410 site–year combinations.

2.1.6 Land cover dataset

To avoid the impact of human activities and non-vegetated areas on data quality, areas of cropland, cropland/natural vegetation mosaics, permanent snow and ice, barren land and water bodies were removed based on a land cover dataset obtained by supervised classification of MODIS reflectance data (Sulla-Menashe and Friedl, 2018). The land cover data generated based on the Annual International Geosphere–Biosphere Programme classification schemes, are available from https://lpdaac.usgs.gov/products/mcd12q1v061/ (Friedl and Sulla-Menashe, 2022).

2.2 Ensemble method for estimating phenological dates

The weighting method was applied to obtain more accurate SOS and EOS dates from the four vegetation phenology datasets. The weight assigned to each product was based on the interannual variability of each phenology dataset, together with the degree of consistency and offset among the four phenology datasets (Giorgi and Mearns, 2002). There is discrepancy in the spatial coverage among the four phenology datasets, and missing data occurs in specific regions for some of the datasets. The ensemble method can fill in missing data accurately, thereby producing a phenology dataset with high accuracy and spatially continuous coverage. Furthermore, the process of merging the phenology datasets does not depend on simple averaging; instead, it is based on the uncertainty among the products, which produces data that is more reliable than those obtained using the simple averaging method, and can circumvent the effects of outliers (Giorgi and Mearns, 2002).

2.2.1 Reliability ensemble averaging method

The weighting method was applied to obtain more accurate SOS and EOS dates from the four vegetation phenology datasets. The weight assigned to each product was based on the interannual variability of each phenology dataset, together with the degree of consistency and offset among the four phenology datasets (Giorgi and Mearns, 2002). The consistency is measured as the difference between the input dataset and the mean value of the four datasets, and the offset is measured by the difference between the REA result and each input dataset, they are calculated in iterations. There are~~is~~ discrepancies~~y~~ in the spatial coverage among the four phenology datasets, and missing data occurs in specific regions for some of the datasets. The ensemble method can fill in missing data accurately, thereby producing a phenology dataset with high accuracy and spatially continuous coverage. Furthermore, the process of merging the phenology datasets does not depend on simple averaging; instead, it is based on the uncertainty among the products, which produces data that is more reliable than those obtained using the simple averaging method, and can circumvent the effects of outliers (Giorgi and Mearns, 2002).

The REA method based on the "voting principle" (-the REA result is generate based on different weights of data sources) generates data that is consistent with most of the input phenology products at the pixel level. It provides a dataset with high reliability by relying on the temporal consistency of each pixel among the input products, and by minimizing the influence of outliers during the merging process (Giorgi and Mearns, 2002). The REA method has been applied to generate datasets for multiple elemental fields, e.g., temperature, evapotranspiration, and precipitation (Giorgi and Mearns, 2002; Lu et al., 2021; Xu et al., 2010). In this study, the REA method was used to integrate both the SOS and the EOS from the four phenology datasets.

The REA method gives different weights to the various datasets involved in the process of data merging, and then obtains the desired result using the following function:

$$\widehat{\Delta Phe} = \tilde{A}(\Delta Phe) = \frac{\sum_i R_i \Delta Phe_i}{\sum_i R_i} \tag{1}$$

where $\widehat{\Delta Phe}$ represents the phenology result, ΔPhe_i represents the different datasets involved in the process, $\tilde{A}$ denotes the REA process, and R_i represents the model reliability factor, which is defined as follows:

$$R_i = \left[\left(R_{B,i} \right)^m \times \left(R_{D,i} \right)^n \right]^{\left[\frac{1}{m \times n} \right]}$$

$$= \left\{ \left[\frac{\epsilon_{Phe}}{abs(B_{Phe,i})} \right]^m \left[\frac{\epsilon_{Phe}}{abs(D_{Phe,i})} \right]^n \right\}^{\left[\frac{1}{m \times n} \right]} \tag{2}$$

where $R_{B,i}$ measures the bias of the data compared with that of the average data (the higher the bias, the lower the reliability of the dataset), and $R_{D,i}$ represents the convergence criterion of the data (the larger the distance between the dataset and the newly generated REA data, the poorer the convergence; several iterations are required to reach convergence). The values of $R_{B,i}$ and $R_{D,i}$ will be set to 1 when $B_{Phe,i}$ and $D_{Phe,i}$ are less than ϵ_{Phe}, which means the deviation of the dataset is within the limit of natural variation.

$$B_{Phe,i} = \Delta Phe_i - \overline{Phe}, \tag{3}$$

$$D_{Phe,i} = \Delta Phe_i - \Delta Phe, \tag{4}$$

$$\varepsilon_{Phe} = \max\big(MA(D_{Phe})\big) - \min\big(MA(D_{Phe})\big). \tag{5}$$

Equation (3) explains the derivation of $B_{Phe,i}$ i.e., it is defined by the difference between the input dataset and the mean value of the four datasets. Equation (4) explains the arithmetic process of $D_{Phe,i}$, which is measured by the difference between the REA result and each input dataset. In Eq. (5), ε_{Phe} is measured by the natural variability in phenology, which is calculated by estimating the difference between the maximum and minimum values of the multiyear moving averages following linear detrending of the observed long-term series data, and works with $B_{Phe,i}$ and $D_{Phe,i}$ jointly to assign weights to each dataset. Natural variability changes from region to region, in Equation (1) and (6), ε_{Phe} cancels out under the condition of $B_{Phe,i}$ and $D_{Phe,i}$ greater than ε_{Phe}, which based on the assumption that more stringent on are required to increase the reliability over regions characterized by lower natural variability.

$$\delta_{Phe} = \left[\tilde{A}\big(\Delta Phe_i - \widetilde{\Delta Phe}\big)^2\right]^{\frac{1}{2}} = \left[\frac{\sum_i R_i\big(\Delta Phe_i - \widetilde{\Delta Phe}\big)^2}{\sum_i R_i}\right]^{\frac{1}{2}} \tag{6}$$

$$\Delta Phe_+ = \widetilde{\Delta Phe} + \tilde{\delta}_{\Delta Phe}, \tag{7a}$$

$$\Delta Phe_- = \widetilde{\Delta Phe} - \tilde{\delta}_{\Delta Phe}. \tag{7b}$$

In Eq. (6), δ_{Phe} is the uncertainty range calculated using R_i and the difference between the REA result and the datasets (a higher value of δ_{Phe} means larger differences between the REA result and the original phenology datasets). The upper and lower ~~limits of the~~ uncertainty ~~range~~ limits are measured by $\widetilde{\Delta Phe}$ and $\tilde{\delta}_{\Delta Phe}$, respectively, in Eqs. (7a) and (7b).

If there is one data that shows significant discrepancies compared to other data, which may cause by improper extraction methods in that region, the $B_{Phe,i}$ and $D_{Phe,i}$ will extract this variance and combine with the natural variability ε_{Phe} of the region in the weight distribution process. If the natural variability of that region is low, then the weight is assigned to a smaller value, and if the natural variability of the region is large, the weight is assigned by both the natural variability and the deviations.

2.2.2~~3~~ Evaluation criteria

In this study, the metrics of the root mean square error (RMSE), BIAS, correlation coefficient (r), unbiased RMSE (UbRMSE) and coefficient of variation (CV) were used for data evaluation:

$$RMSE = \sqrt{\frac{\sum_{i=1}^{n}(Phe_i - Ref_i)^2}{n}}, \tag{8}$$

$$BIAS = \frac{\sum_{i=1}^{n}(Phe_i - Ref_i)}{n}, \tag{9}$$

$$r = \frac{\sum_{i=1}^{n}\big(Phe_i - \overline{Phe}\big)\big(Ref_i - \overline{Ref}\big)}{\sqrt{\sum_{i=1}^{n}\big(Phe_i - \overline{Phe}\big)^2}\sqrt{\sum_{i=1}^{n}\big(Ref_i - \overline{Ref}\big)^2}}, \tag{10}$$

$$ubRMSE = \sqrt{RMSE^2 - BIAS^2}, \tag{11}$$

$$STD = \sqrt{\frac{1}{N}\sum_{i=1}^{N}\left(Phe_i - \overline{Phe}\right)^2}, \tag{12}$$

$$CV = \frac{\sigma_{Phe}}{\overline{Phe}} \tag{13}$$

where n represents the number of site years, Phe_i represents the corresponding vegetation phenological indicator (i.e., SOS and EOS) at a given point, Ref_i represents data from a phenology camera, σ_{Phe} represents the standard deviation of Phe_i, and $\overline{Phe}$ and $\overline{Ref}$ represent the average of Phe_i and Ref_i, respectively.

RMSE is calculated as the square root of the average of the squares of the residuals, which penalizes larger errors than smaller ones and provide an estimate of the magnitude of errors between remote sensing estimated value and phenocam datasets. BIAS is the average difference between remote sensing estimated value and phenocam value, that helps in understanding whether the estimated value is higher or lower than phenocam value. The correlation coefficient measures the linear relationship between two variables. The ubRMSE measures the deviation between two variables without systematic errors. Standard deviation quantifies the variation of the dataset, which measures the deviation between data and the mean value.

2.2.~~3~~4 Mann–Kendall trend test

The Mann–Kendall trend test is a nonparametric trend test method, which has the characteristics of not being limited by a specific distribution and a small number of outliers, and can be used to detect the hypothesis trend of time series data (Kendall, 1975~~; Mao et al., 2022; Sun et al., 2019~~). The M-K test is applied to analyze the trend of SOS and EOS during 1982-~~2022~~ 2020 in the merged dataset. The basic Mann–Kendall test formulas are as follows:

$$S = \sum_{i=1}^{n-1}\sum_{j=j+1}^{n} sgn(X_j - X_i), \tag{14}$$

$$Z_c = \begin{cases} \dfrac{S-1}{\sqrt{Var(S)}} & S > 0 \\ 0 & S = 0 \\ \dfrac{S+1}{\sqrt{Var(S)}} & S < 0 \end{cases} \tag{15}$$

where X_i and X_j are the phenological parameter values of the i-th year and the j-th year of the pixel, respectively, n is the length of the time series, sgn is the sign function, and S is the test statistic. The null hypothesis H_0: the time series data is n independent samples with identically distributed random variables, H_1: for any $i, j \leq n$, and $i \neq j$, the distribution of X_i, X_k is different. If $|Z| \geq Z_{1-\frac{\alpha}{2}}$, the time series is considered to have a statistically significant change; otherwise, any change is considered not statistically significant. When $Z > 0$, the time series has an upward trend; when $Z < 0$, it has a downward trend (Zhou and Liu, 2018).

3 Results

3.1 Difference in vegetation phenological dates among the four datasets

Figure 1 illustrates the spatial distribution of the multiyear mean dates for both the SOS and the EOS above 30°N for each of the four datasets. The mean SOS values for the MCD12Q2, VIP, GIM_3g, and GIM_4g datasets are day of the year (DOY) 120 (std = 32 d), 125 (std = 43 d), 132 (std = 17 d), and 139 (std = 32 d), respectively. Discrepancies among the datasets are particularly notable in southwestern North America, North Africa, the Qinghai–Tibet Plateau, and Mongolia. Compared with the SOS, the EOS exhibits greater variability, and the mean EOS values for the MCD12Q2, VIP, GIM_3g, and GIM_4g datasets are DOY 281 (std = 37 d), 290 (std = 44 d), 315 (std = 19 d), and 287 (std = 53 d), respectively. Among the four datasets, the spatial distributions of the GIM_4g and VIP datasets are the most similar. In comparison with these two datasets, the MCD12Q2 dataset displays lower EOS values in Northern Europe, Central Asia, North America, and in the 45°–60°N latitudinal belt over Central Asia. Given the substantial differences among these datasets, it is imperative to integrate these datasets into a merged dataset with higher accuracy.
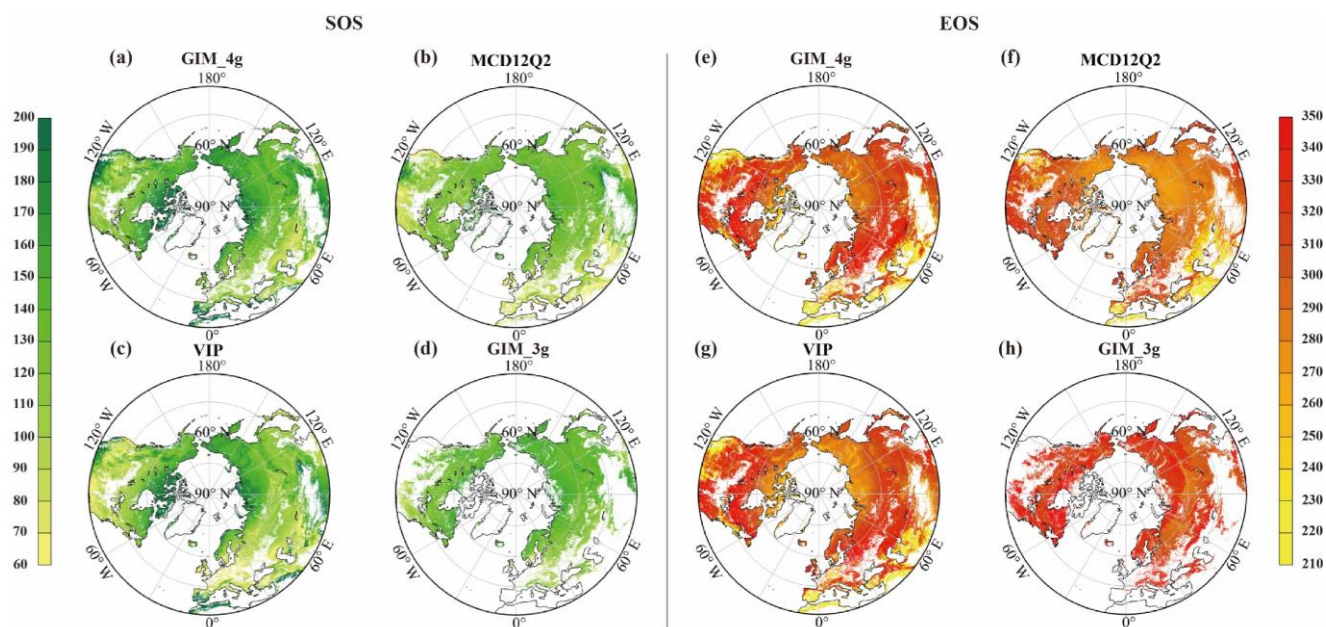
Figure 1: Spatial distribution of multiyear mean SOS and EOS dates from each phenology dataset: (a–d) multiyear mean SOS dates and (e–h) multiyear mean EOS dates derived from the GIM_4g, MCD12Q2, VIP, and GIM_3g datasets, respectively.

3.2 Variation of weights and contributions of the four datasets to the merged phenology dataset

The weight of each dataset, as determined by the REA method, varies largely among years and specific locations. The left panels of Fig. 2 illustrate the mean weight for each dataset in each year over the period 1982–20222020, with the upper and lower sections representing the SOS and the EOS, respectively. For the SOS, the overall weight of the VIP dataset during 1982–1998 surpasses that of the GIM_4g dataset. The GIM_3g dataset is dominant during 1999–2014, with weights exceeding

65%. In 2015, the weighting of the MCD12Q2 dataset was highest at approximately 45%, with the weights of the other two datasets broadly similar. During 2016–2020, the weights of the MCD12Q2 and GIM_4g datasets are 61% and 39%, respectively~~, but during 2021–2022, the dataset consists solely of the MCD12Q2 dataset~~. The combinations of data sources for the EOS data are similar to those for the SOS data. Specifically, during 1982–1998, the weight of the VIP dataset is approximately 65%, with the GIM_4g dataset accounting for the remaining 35%. For 1999–2000, the weighting of the GIM_3g dataset is approximately only 10%, whereas that of the VIP dataset is the highest (approximately 55%). Throughout the period 2001–2014, the weighting of the VIP dataset is greatest (>45%), whereas that of the GIM_3g dataset is low (<10%); the weighting of the GIM_4g and MCD12Q2 datasets each account for over 20%. During 2016–2020, the weights of the GIM_4g and MCD12Q2 datasets are broadly equal, albeit with the weighting of the GIM_4g dataset slightly exceeding that of the MCD12Q2 dataset.

The latitudinal distribution of the mean weighting of the datasets for the SOS and the EOS is shown in Fig. 2(b) and 2(d), respectively. For the SOS data, the zonal distribution of the GIM_4g, VIP, and MCD12Q2 datasets is reasonably stable within 30°–75°N. The weight of the GIM_3g dataset is notably higher between 50°N and 70°N, primarily because of its spatial distribution, and it shows notable fluctuations in high-latitude areas. In contrast, the weighting of the EOS datasets exhibits relatively smooth changes within 30°–75°N. There are marked fluctuations in the weighting of the GIM_4g and VIP datasets in high-latitude areas above 75°N. The weight of the GIM_4g dataset between 30°N and 75°N fluctuates before stabilizing smoothly. Conversely, the weight of the VIP dataset increases with latitude, displaying a trend opposite to that of the GIM_4g dataset. Additionally, the weighting of both the MCD12Q2 and the GIM_3g datasets initially increases and then decreases with increasing latitude.

295
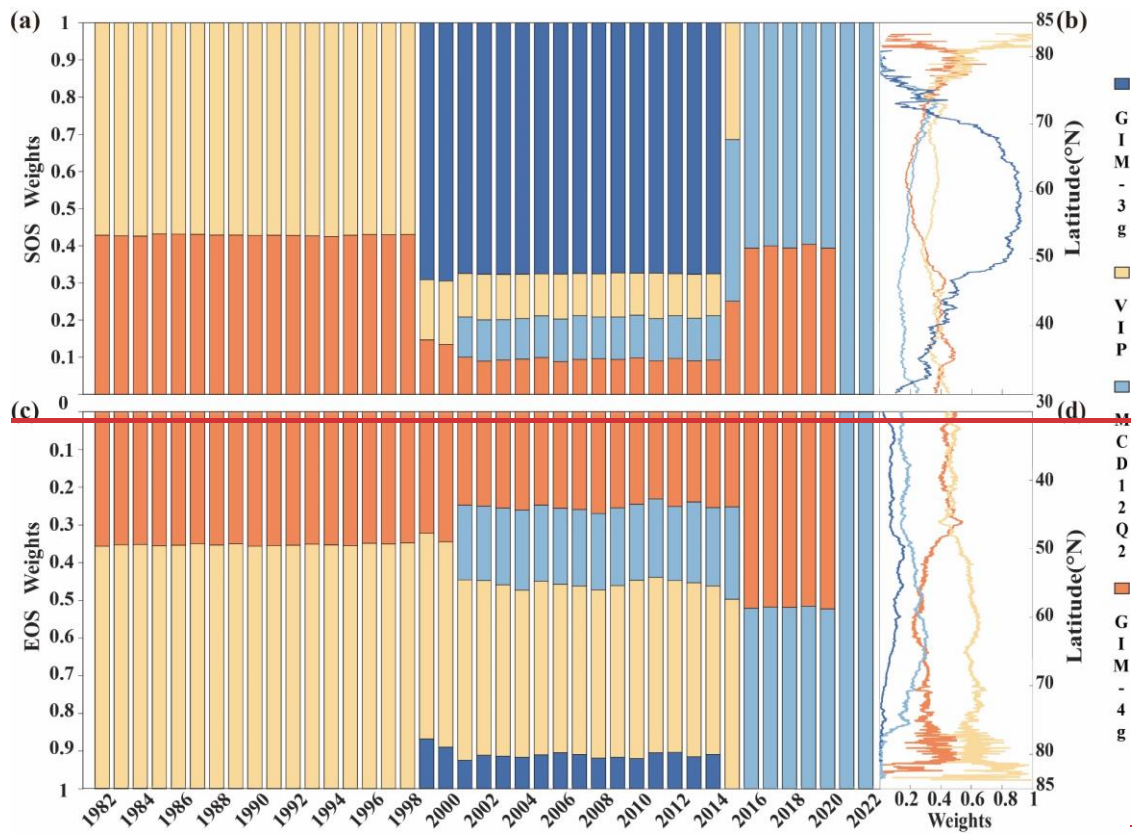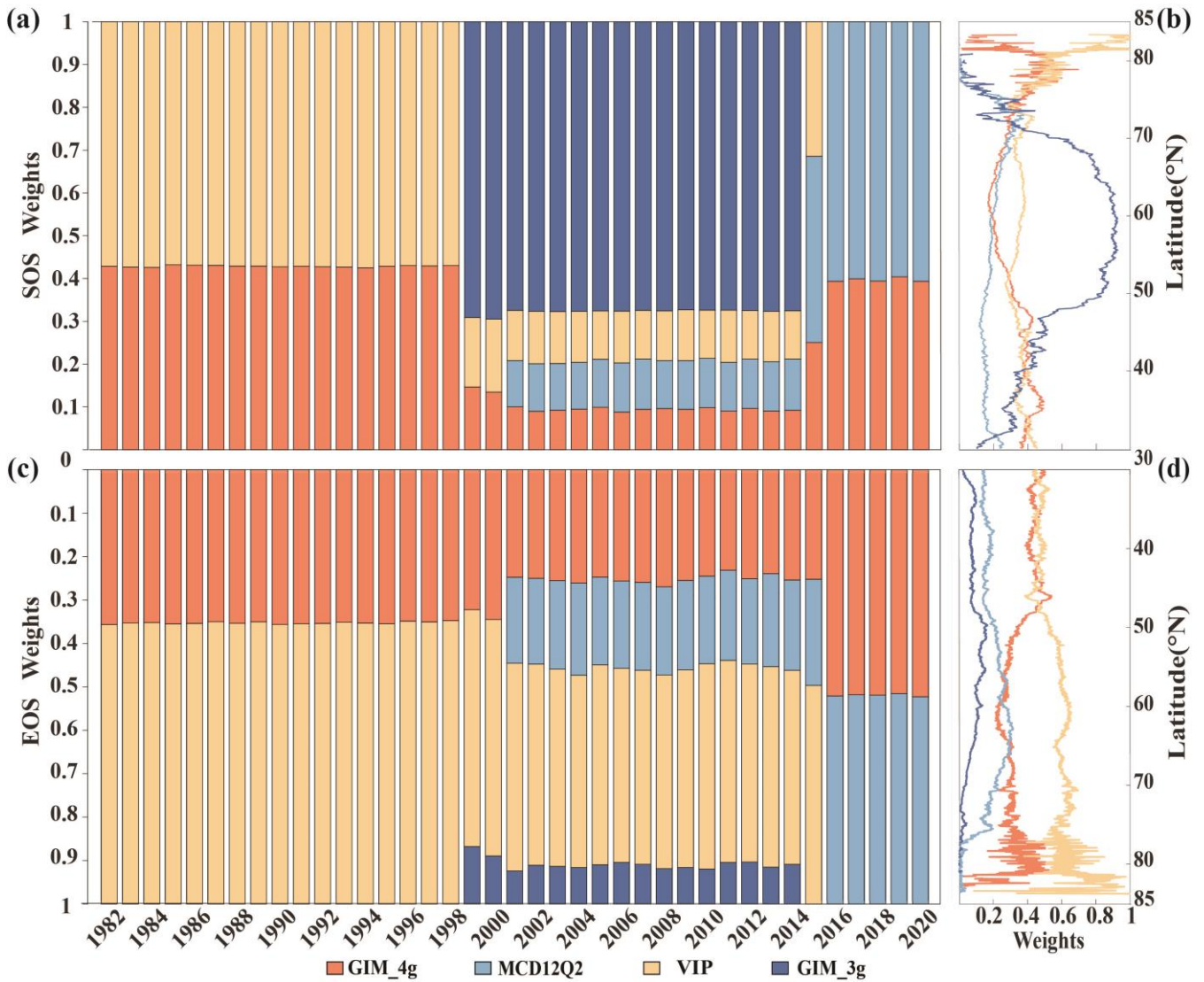
Figure 2: (a and c) Weights of the four phenology datasets during 1982–~~2022~~ 2020 and (b and d) latitudinal differences for (a and b) the SOS and (c and d) the EOS. The four datasets comprise the GIM_4g, MCD12Q2, VIP, and GIM_3g datasets (for the full names, see Table 1).

Figure 3 shows the spatial distribution of the mean contribution of the four datasets to the merged SOS and EOS results, calculated as the average weight for each pixel over the timespan for the corresponding dataset. For the SOS data, the GIM_3g dataset exhibits the greatest contribution, followed by similar contributions from the GIM_4g and VIP datasets; the MCD12Q2 dataset has the smallest contribution. The MCD12Q2 dataset has a greater contribution in high-latitude areas near the Arctic Circle, but makes a smaller contribution in most other regions. The VIP dataset generally has a greater contribution than that of the MCD12Q2 dataset, with values ranging between 0 and 0.5 in 90% of areas. The overall contribution of the GIM_3g dataset is reasonably uniform, averaging at approximately 0.37. For the EOS data, the VIP dataset has the greatest contribution,

followed by the GIM_4g dataset; the GIM_3g dataset has the smallest contribution. The contribution of the MCD12Q2 dataset remains relatively small, primarily distributed between 0 and 0.5. The VIP dataset has a positive correlation with latitude, with approximately 4.7% of areas of weights exceeding 0.8 in central Asia and parts of East Asia, whereas the contribution of the GIM_3g dataset remains lower across the entire region.
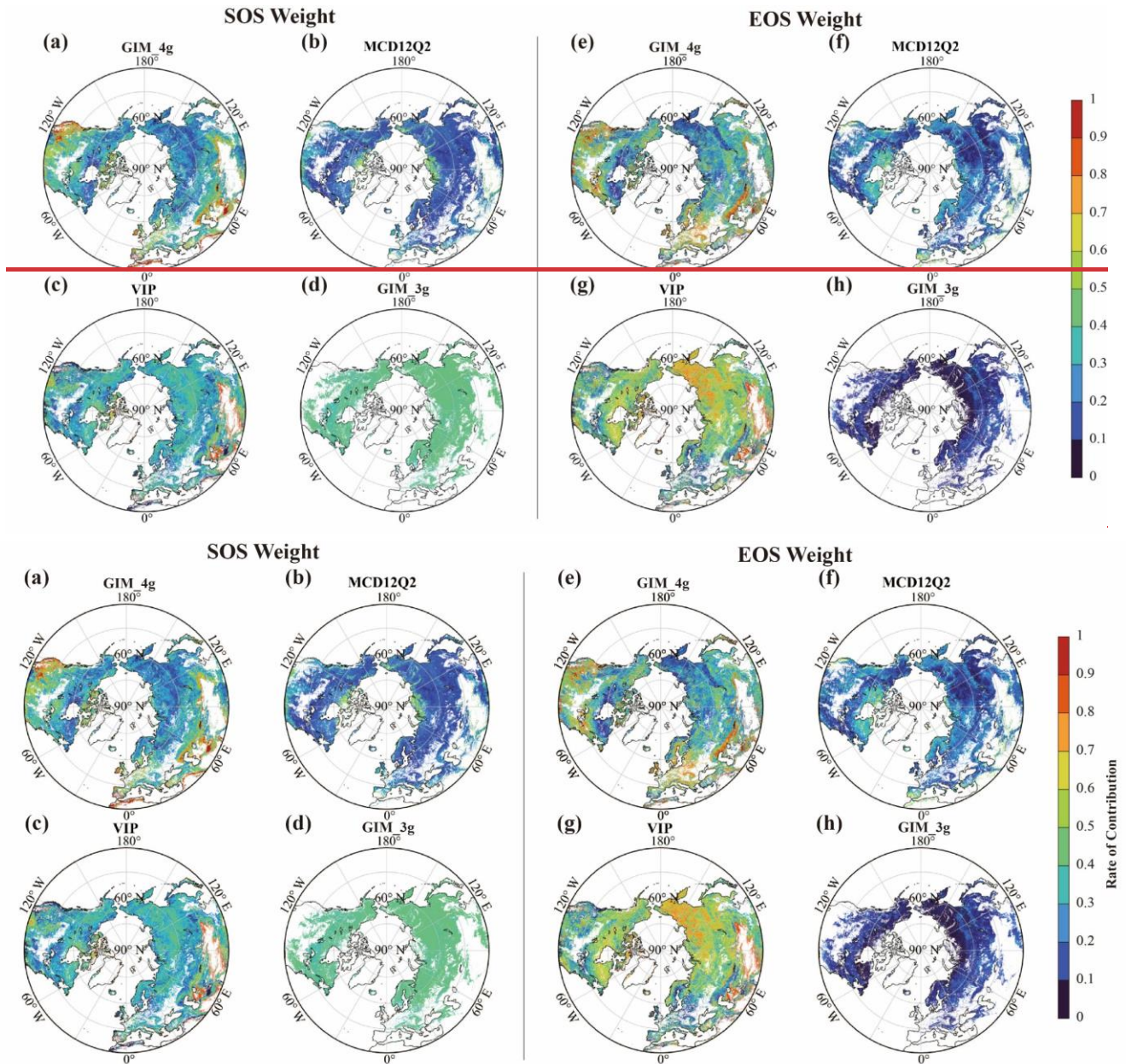
Figure 3: Spatial distribution of the mean contribution of the four datasets to the merged SOS and EOS results. (a–d) The mean SOS weight derived from the GIM_4g, MCD12Q2, VIP, and GIM_3g datasets, respectively, and (e–h) the mean EOS weight derived from the GIM_4g, MCD12Q2, VIP, and GIM_3g datasets, respectively.

3.3 Merged phenology dataset using the REA method

Figure 4 displays the merged mean SOS and EOS dates for the period 1982–~~2022~~2020. For the SOS, a general pattern of increase with latitude is evident, albeit with later occurrence of the SOS in southwestern North America, on the Qinghai–Tibet Plateau~~, etc~~. The highest proportion of the SOS falls within DOY 120–150 (40.0%), followed by DOY 90–120 (23.3%). The probabilities of the SOS within the intervals of DOY 60–90 and DOY 150–180 are comparable, i.e., 14.8% and 15.8%, respectively, with only 6.2% of areas experiencing the SOS later than DOY 180. The mean SOS obtained using the REA method is DOY 129 (std = 28 d). It demonstrates an overall increase in the EOS with latitude, with fewer trends observed in high-latitude areas above 60°N and eastern parts of North America. The distribution of the EOS appears more uniform after merging. Unlike the SOS data, the EOS primarily occurs within DOY 270–330 (93.1%). The mean EOS is DOY 283 (std = 23 d). Interannual variability in most regions for both the SOS and the EOS data is minimal; however, notable variations are observed in areas such as southwestern North America, Spain, Portugal, North Africa, West Asia, and Mongolia, consistent with the earlier analysis of data sources(Fu et al., 2014; Liu et al., 2016; Piao et al., 2006, 2015).

The mean uncertainty range of merged SOS and EOS dates, calculated using Equation (6), is presented in Figure 4. This range was determined using the REA method over the period from 1982 to 2020.~~The mean uncertainty range (by Equation 6) of merged SOS and EOS dates and its coefficient of variation (CV) using the REA method during 1982–2022 are presented in Figure 4.~~ The mean uncertainty range of SOS (EOS) dates is below 10d in more than 96% (94%) of regions, with less than 4% (5%) of regions exhibiting a mean uncertainty range exceeding 10d or 15d Fig. 4(b, e). The mean uncertainty range of SOS dates shows a negative correlation with latitude, whereas this trend is not evident in EOS dates. In Fig. 4(c, f), regarding the coefficient of variation (CV) in the uncertainty range of SOS (EOS) dates from 1982 to ~~2022~~2020, more than 56% (73%) of regions have a CV below 1, 31% (18%) regions have a CV between 1 and 1.5, and only 13% (8%) of regions have a CV higher than 1.5. ~~Regions with a CV below 1 in the uncertainty range of SOS and EOS dates are mostly located in the middle latitudes, but n~~There is no ~~observable~~ evident correlation between CV and latitude changes~~ is evident~~.
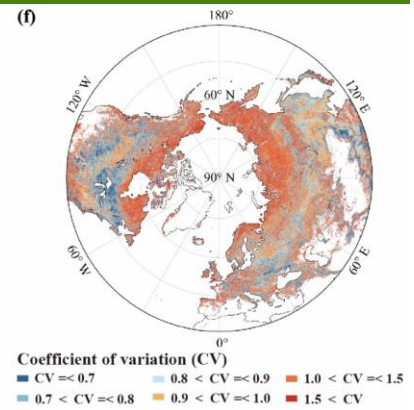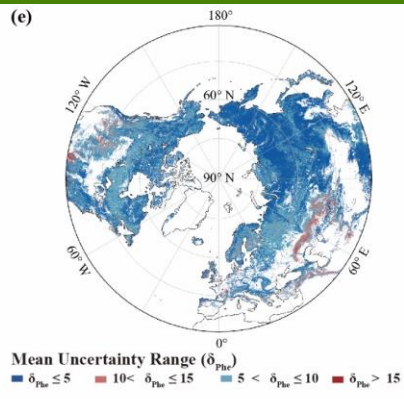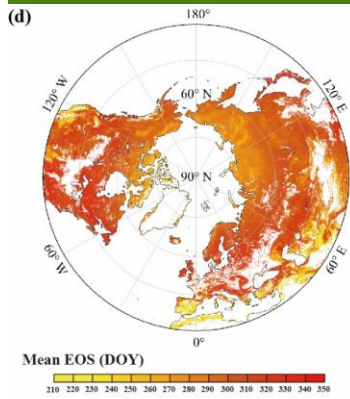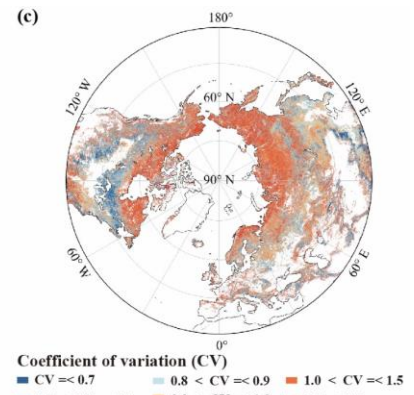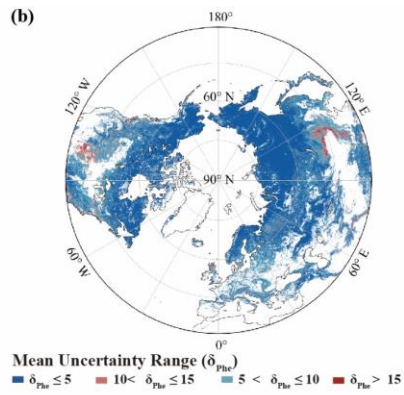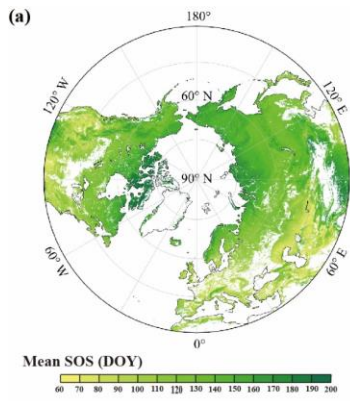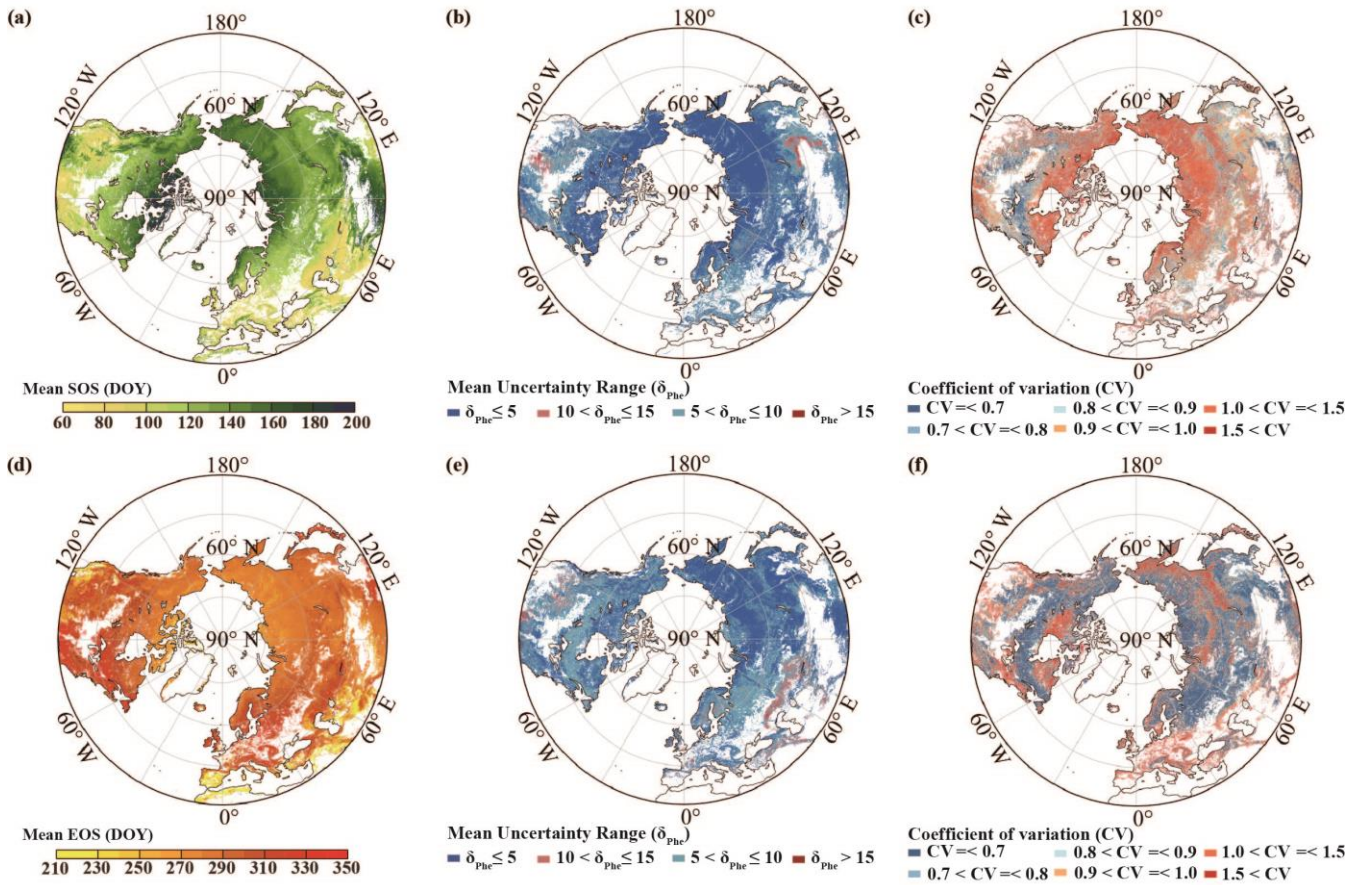
Figure 4: Merged mean (a) SOS and (db) EOS dates (DOY) obtained using the REA method for the period 1982– 2022 2020 and the uncertainty in the REA merged data. Mean uncertainty (δ_{Phe}) of SOS dates (b) and EOS (e) obtained using the REA method for the period 1982– 20222020, and its coefficient of variation (CV) in merged SOS (c) and EOS dates (f).

The pPhenocCam dataset was used to evaluate each of the four vegetation datasets and the merged dataset. Verification results of the SOS and EOS data indicate that the merged data produced using the REA method has the best performance (Fig. 5). Specifically, the RMSE for the SOS and the EOS is 12 and 17 d, respectively. The correlation between the SOS and pPhenocCam results is notably high at 0.84; for the EOS, it is 0.71. Evaluation of the four satellite-based SOS products shows that the GIM_3g dataset has the highest correlation coefficient and the lowest RMSE among the four datasets. However, it has more missing values spatially and a shorter time span, leading to fewer points for verification. The MCD12Q2 dataset has a correlation coefficient of 0.65 and an RMSE of 20 d, but its wider spatial coverage provides more points for verification. The GIM_4g dataset has a lower correlation with the pPhenocCam dataset owing to outliers, resulting in an RMSE of 29 d. Compared with the pPhenocCam dataset, the VIP dataset has a lower estimation in the SOS range of DOY 100–140, leading to a larger RMSE. And comparing with simple average, the REA-based SOS shows better performance in RMSE (REA and Average, 12d and 21d, respectively), CORR (REA and Average, 0.84 and 0.65, respectively), BIAS (REA and Average, -1.5d

and -9.7d, respectively) and UbRMSE (REA and Average, 12d and 18d, respectively). The REA-based SOS dataset outperforms in terms of all indicators, with the lowest RMSE, UbRMSE, and standard deviation, together with the highest correlation and lowest absolute bias, thereby demonstrating high consistency with the pPhenocCam dataset.

In the evaluation of the EOS, the MCD12Q2 dataset has the best results among the four datasets, and except for the REA result, it has the highest correlation coefficient and the lowest RMSE. The GIM_4g dataset shows good performance but tends to overestimate the EOS, resulting in an RMSE of 43 d. Both the VIP and the GIM_3g datasets overestimate the EOS owing to their spatial and temporal distributions, with RMSEs of 46 and 35 d, respectively. The REA-based EOS also shows better performance in RMSE (REA and Average, 17d and 32d, respectively), CORR (REA and Average, 0.71 and 0.45, respectively), BIAS (REA and Average, 1.0d and 8.0d, respectively) and UbRMSE (REA and Average, 17d and 31d, respectively). It is evident from Fig. 5 that the REA dataset demonstrates the highest accuracy and best consistency with the pPhenocCam dataset, outperforming the four other datasets in terms of all indicators, with the lowest RMSE, UbRMSE, and standard deviation, together with the highest correlation and lowest absolute bias.
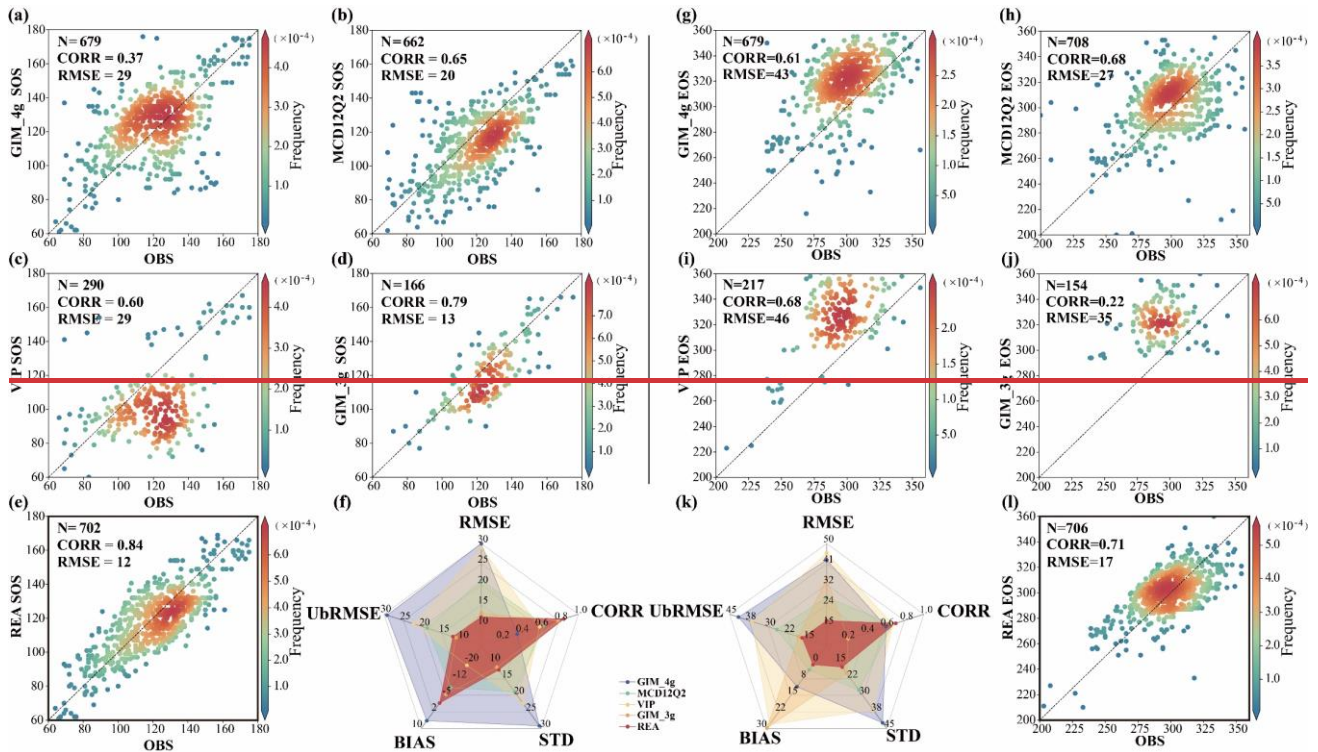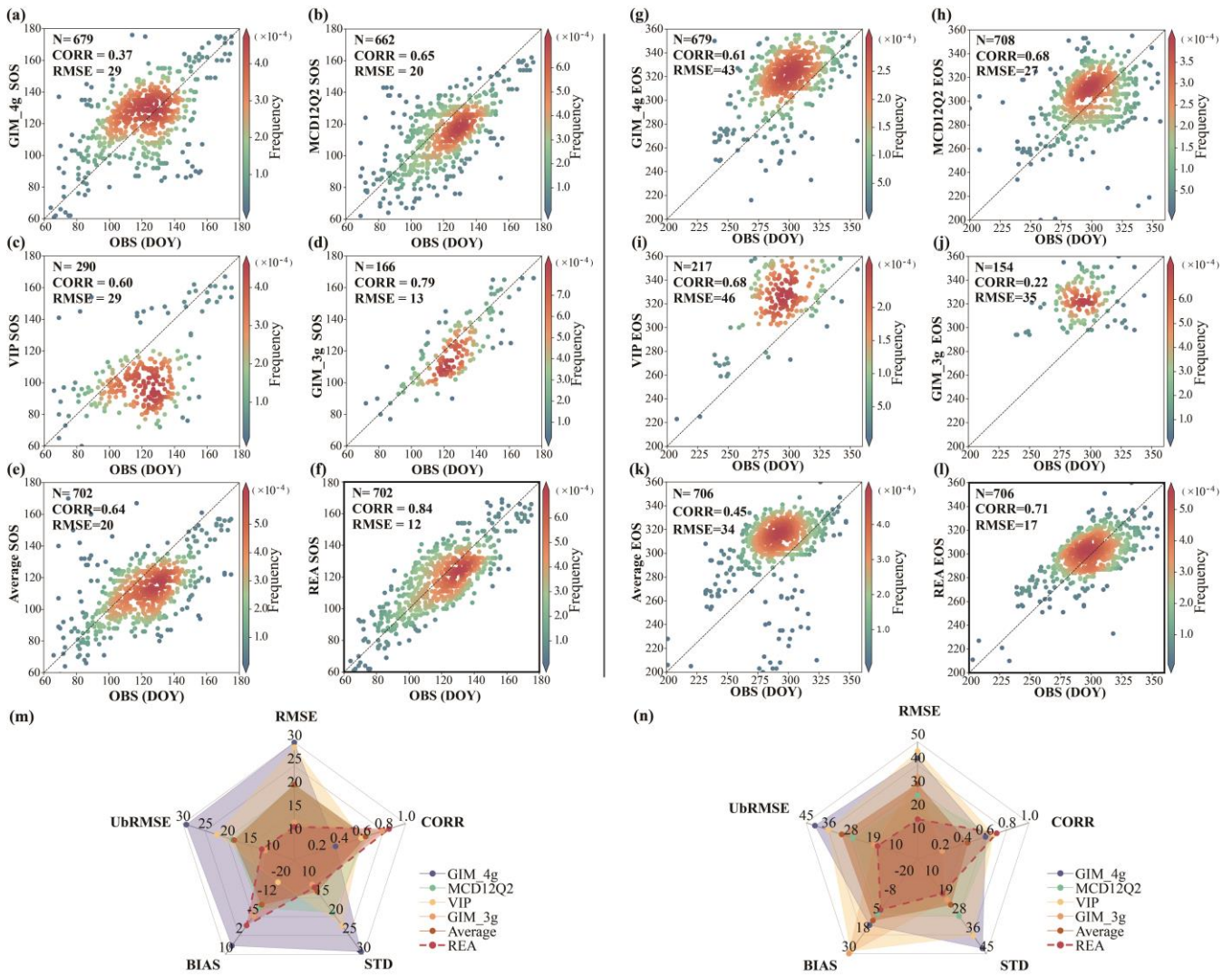
Figure 5: Scatterplots and radar charts of performance for each phenology dataset and the merged phenology dataset obtained using the REA method. (a~~e~~f**)** SOS evaluation results of the GIM_4g, MCD12Q2, VIP, GIM_3g, Average, and REA datasets, respectively, (~~f~~m) radar chart of the SOS evaluation results, (g~~j and~~l) EOS evaluation results of the GIM_4g, MCD12Q2, VIP, GIM_3g, Average, and REA datasets, respectively, and (~~k~~n) radar chart of the EOS evaluation results. Each point represents a site year in the figure. OBS indicates ground-based ~~p~~Phenoc~~C~~am phenological dates, RMSE indicates the root mean square error, UbRMSE indicates the unbiased RMSE, BIAS indicates the mean difference between the satellite-based results and the ground-based verification results, ~~and~~STD indicates the standard deviation, and CORR indicates the correlation coefficient.

~~Due to differences in time scales between p~~Phenoc~~C~~am data and different phenology datasets, w~~We selected a long-term ~~p~~Phenoc~~C~~am site (Morganmonroe) from PhenoCam ~~that aligns with the time span of these phenology datasets~~ to evaluate the merged dataset. We have chosen an ~~American~~US. PhenoCam site characterized by deciduous broad-leaved forest and the time range is ~~2002~~200910-~~2010~~20~~18~~20 for SOS and ~~2008~~20101-~~2009~~20~~18~~20 for EOS. As shown in the time series plot in Figure ~~6~~S4, the consistency between the REA and PhenoCam data for both SOS and EOS compared to other datasets is the largest.

380   Additionally, most vegetation phenology products demonstrate higher consistency with PhenoCam data for SOS compared to EOS.
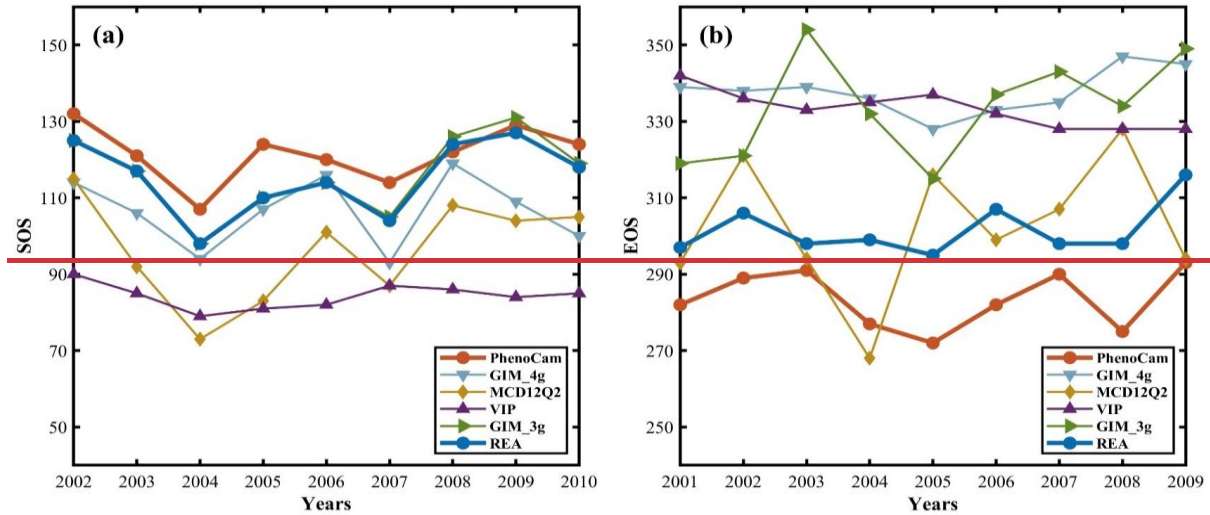
~~Figure 6: Time series of a PhenoCam~~ Morganmonroe~~site data with each phenology dataset and the merged phenology dataset obtained using the REA method. (a) SOS time series of the PhenoCam, GIM_4g, MCD12Q2, VIP, GIM_3g, and REA datasets, respectively, (b) EOS time series of the PhenoCam, GIM_4g, MCD12Q2, VIP, GIM_3g, and REA datasets, respectively.~~

3.4 Temporal trends of phenology based on the merged dataset

It is evident from Fig. ~~7~~6(a) that the SOS exhibits a significant ($p < 0.01$) trend of advance (earlier dates in SOS) ~~–~~over the period 1982–~~2022~~2020, with a rate of advance of approximately 0.~~24~~19 d yr^{-1}. Fig~~ure~~ ~~7~~6(b) presents the spatial distribution of the SOS trends obtained using the Mann–Kendall test. Approximately 6~~45~~.~~37~~58% of the regions exhibit a trend of advance, with 4~~46~~.~~88~~25% ~~of regions~~ exhibiting a significant ($p < 0.05$) trend, while 18.53% of regions demonstrate a significant trend of delay (later dates in SOS).

Fig~~ure~~ ~~7~~6(c) illustrates that the EOS exhibits a significant trend of delay (later dates in EOS) with a rate of 0.1~~6~~8 d yr^{-1} ($p < 0.01$). It is evident from Fig. 7(d) that the proportion of areas experiencing delayed EOS in regions above 30°N is 6~~86~~.~~11~~08% (comprising 4~~63~~.~~60~~21% significant at $p < 0.05$), consistent with the corresponding trend depicted in Fig. ~~7~~6(c). Apart from southwestern to northeastern regions of North America, Europe, the Middle East, and certain high-latitude areas in Asia, EOS delay is predominant. Over the study area, 46.72~~45.69~~% of regions exhibit SOS advance and EOS delay, 17.73~~18.97~~% show SOS advance and EOS advance, 21.42~~19.49~~% demonstrate SOS delay and EOS delay, and 14.~~42~~14% show SOS delay and EOS advance.

400
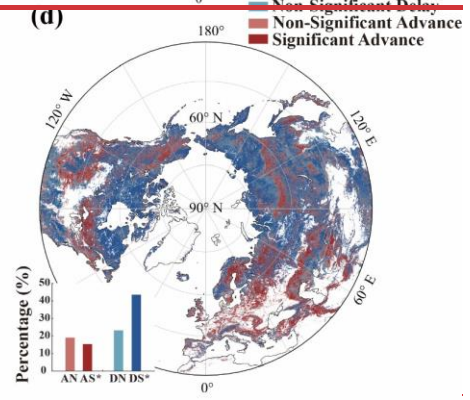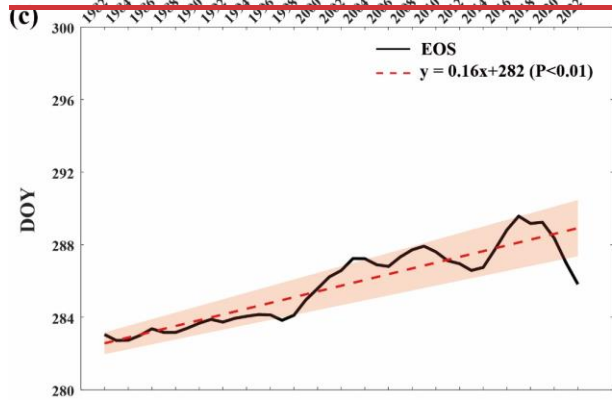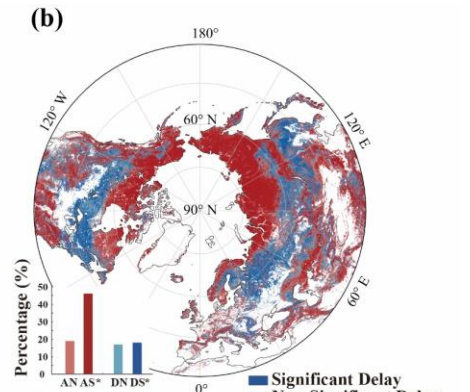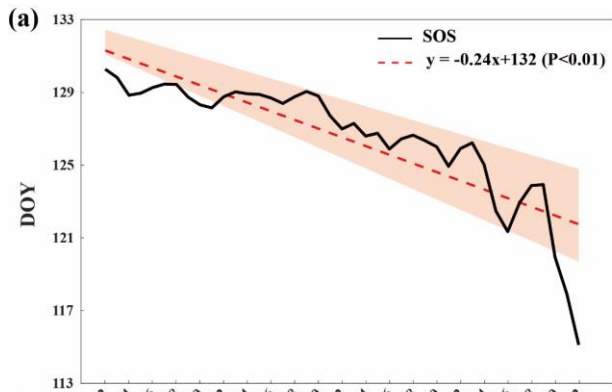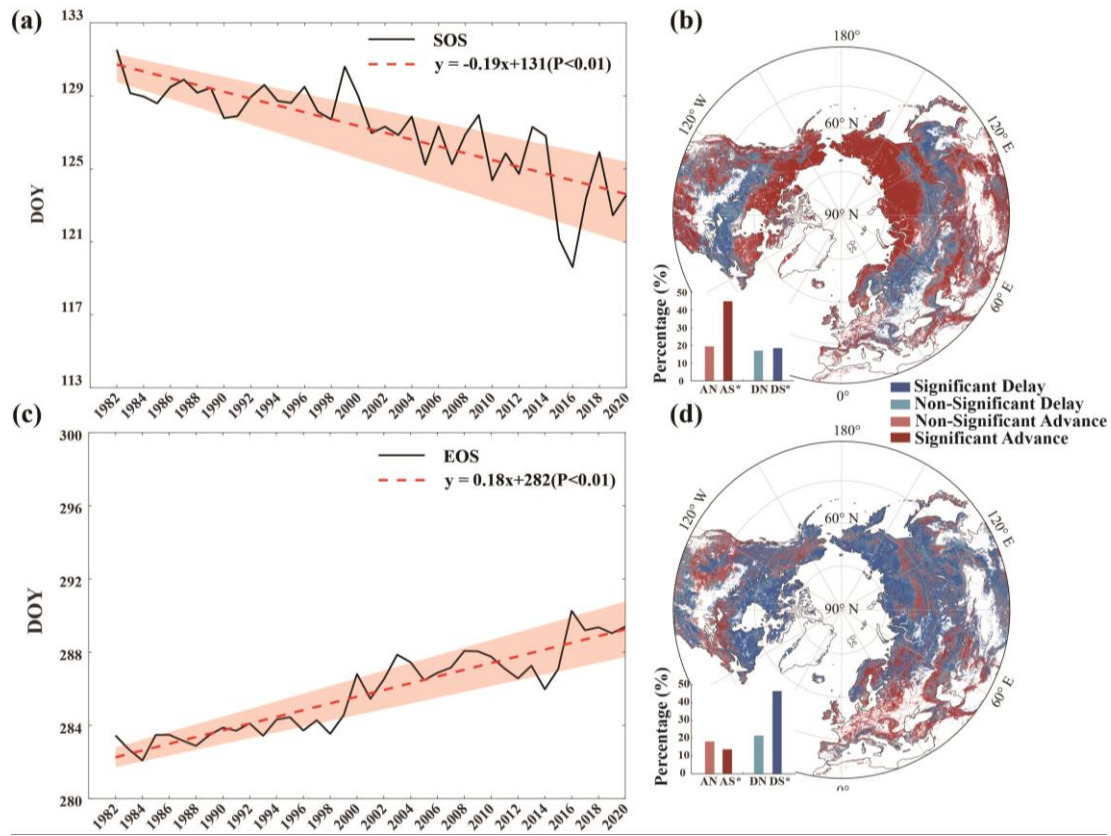
Figure 6: Temporal and spatial trends of the SOS and the EOS over the period 1982–2020 based on the merged dataset obtained using the REA method. (a) Temporal trend of the SOS over the period 1982-2020, (b) Spatial trend of the SOS over the period 1982-2020, (c)Temporal trend of the EOS over the period 1982-2020, (d) Spatial trend of the EOS over the period 1982-2020. The shaded area in (a) and (c) indicates uncertainty at one standard deviation, red lines in (a) and (c) are the fitting lines of average SOS/EOS dates for each year, and black lines are the average SOS/EOS date for each year. Significant delay (DS), non-significant delay (DN), significant advance (AS), non-significant advance (AN).

~~Figure 7: Temporal and spatial trends of the SOS and the EOS over the period 1982-2022 based on the merged dataset obtained using the REA method.~~ ~~(a) Temporal trend of the SOS over the period 1982-2022, (b) Spatial trend of the SOS over the period 1982-2022, (c)Temporal trend of the EOS over the period 1982-2022, (d) Spatial trend of the EOS over the period 1982-2022. The shaded area in (a) and (c) indicates uncertainty at one standard deviation.~~

4 Discussion and Conclusions

Different vegetation phenology datasets have been produced and ~~were~~ are widely used, but we found that differences of more than two months (>60 d) exist in key phenological dates among these datasets, consistent with previous reports (White et al., 2009; Zeng et al., 2020). Remote sensing vegetation phenology typically reflects transition dates in the vegetation growth cycle, such as the start (budburst) and end (leaf senescence) of the growing season, and different vegetation indices, e.g. NDVI, LAI and SIF, were used. The phenological dates that were extracted from different methods were supposed to indicate changes in actual physiological conditions as accurately as possible. However, the effectiveness of these methods varies across regions

and time period even, and may not always represent the true vegetation conditions. Such as, different vegetation phenology datasets show different performance across regions and years comparing to the phenocam dates in the Fig. S1. The consistency of VIP and ground phenocam data in the year 2001 of deciduous broadleaf forest is the best, while the consistency of GIM_3g data in the year 2002 is better than that of VIP data. Comparing to the forest types, the consistency of remote sensing based phenological dates and phenocam data is higher in deciduous broadleaf region when using GIM_3g method, but in evergreen needleleaf when using the MCD method. Therefore, a method that integrates data from different methods based on reliability is feasible. For remote sensing vegetation phenology datasets with different data sources, one of Tthe substantial differences among the various vegetation phenology datasets are related mainly to differences in the remote sensing image and the corresponding terrestrial feature, including spatial and temporal resolutions, extraction methods, spectral response functions, and the complexity of surface backgrounds (Trishchenko et al., 2002; Zhang et al., 2020). For example, phenology datasets with low spatial resolution experience the problem of the mixed-pixel effect, which means unknown composition of vegetation types may appears in the same pixel (Chen et al., 2018), which and can result in large differences in phenological phenological dates compared with those derived using high-resolution phenology datasets. Another main factor that may induct large variation in phenological dates, are the various remote sensing phenology algorithms (time series data processing methods and phenology extraction methods)(Cong et al., 2012; Wu et al., 2021; Zeng et al., 2020). The choice of data processing or smoothing strongly affects the land surface phenology extracted, and will further influence the trend of how phenology change (positive and negative trends can be found in the same dataset with different phenology extraction method) (Misra et al., 2016). The phenology estimates obtained from different extraction methods show significant variation (Cong et al., 2012), and the optimal phenology extraction parameters also differ among various biomes(Piao et al., 2006; Reed et al., 1994). The REA (reliability ensemble averaging) method is used to catch the dates which can best reflects the change of the vegetation growing state based on the assumption that there exists a data source capable of reflecting the vegetation conditions at each grid cell, and different weights assigned to each data are calculated based on their reliability to get the final result. Thus, a merged phenology dataset is required to exploit the advantages of the various phenology datasets available.

Data fusion methods generally include unmixing-based, weight-function-based, and Bayesian-based methods (Gevaert and García-Haro, 2015; Piao et al., 2019a). In the field of vegetation phenology, fusion methods based on raw remote sensing data, such as the Spatial and Temporal Adaptive Reflectance Fusion Model (Gao et al., 2006) and the Enhanced Spatial and Temporal Adaptive Reflectance Fusion Model (Zhu et al., 2010), are generally influenced by complex vegetation types, vegetation growth status, and the process of coefficient determination of different methods determination (Sisheber et al., 2022). These methods are mainly used in a specific region. The reflectance of vegetation endmembers changes nonlinearly (the spectral signals of different land covers mix spatially in a nonlinear manner, causing the spectral response of a single pixel to no longer be a simple linear combination of the endmember spectra) (Ma et al., 2015)(Ma), and likely results in poor performance in vegetation phenology extraction. The REA method is not based on the hypothesis that pixel reflectance changes linearly; instead, it merges annual phenology products directly based on their reliability. Compared with commonly used data

fusion methods, the REA method offers advantages in terms of simplicity and efficiency(Lu et al., 2021), and it considers the reliability of the data, which contrasts with traditional methods that simply calculate the mean value of various data. There is no restriction on the minimum length of the time series, but it should be available to extract the natural variability to maintain accuracy. The simple averaging method treats each data source equally, even though the uncertainties of each dataset are likely to vary across time and space(Lu et al., 2021; Wang et al., 2019), introducing inaccuracy to the merged dataset. The REA method considers the temporal correlation of vegetation phenology data by employing a voting principle (Giorgi and Mearns, 2002), and this approach facilitates convergence of data while retaining differences in terms of the spatial distribution, thereby offering advantages with respect to multisource data fusion.

Compared with individual vegetation phenology datasets, i.e., the MCD12Q2, VIP, GIM_3g, and GIM_4g datasets, our REA-based phenology dataset has a long-term sequence spanning 1982 2022 2020 with a spatial resolution of 0.05°. The REA method facilitates better convergence and produces a unified phenology product with high reliability. To verify the reliability of the merged data product, we compared it against the ground-based pPheno Ccam dataset. Results revealed that the REA-based SOS and EOS exhibit the lowest RMSE and the highest correlation coefficients compared with those of the other four datasets, suggesting that the REA method offers high processing efficiency and accuracy. Global climate change has notably altered the timing of vegetation phenology events, including the advance of the SOS (Piao et al., 2019a) and the delay of the EOS (Piao et al., 2019a). Both advanced spring phenology and delayed autumn phenology were found between REA-based phenological dates and previous studies. But the amplitudes of trends are different among these studies. In details, SOS was found significantly advance at the rate of 0.19 days per year in the REA result during 1982-2020, while the advancing rate of 1.4±0.6 days per decade during 1982-2011 (Wang et al., 2015) and 5.4 days advanced from 1982 to 2008 (Jeong et al., 2011)was also found in previous studies. Similarly, EOS was found significantly delayed at the rate of 0.18 days per year in the REA result over the same period, while the 0.18±0.38 days per year delay was found for 1982-2011 (Liu et al., 2016) and the 6.6 days delay was found from 1982 to 2008 (Jeong et al., 2011) in previous studies. Based on the merged phenology dataset, our results were consistent with those earlier findings, i.e., Oover the long-term period of 1982 2022, advance (delay) in the REA SOS (EOS) has occurred at the rate of 0.24 (0.16) d yr⁻¹. (Piao et al., 2019b)consistent with previous studies, the EOS was found delayed at a rate of approximately 0.18±0.38 days yr⁻¹ from 1982 2011(liu) and also found EOS delayed 4.3 days in 1982 1999 and 2.3 days in 2000 2008(SU JONG), and SOS was found significant advance at the rate of 1.4±0.6 days decade⁻¹ (wangxuhui) from 1982 2011 and also found advanced 5.4 day in 1982 2008(SU JONG).However, there are also deviations between analyses based on REA phenology dataset and other single dataset(Blunden et al., 2023), which may be attribute to the transformation of data sources or differences in the regions analyzed. The entire seasonal trends in vegetation greenness were estimated, e.g. the NDVI trends (Li et al., 2023), for VIP, GIM_4g and REA method, please see the results in Fig. S2. The average greening trend in VIP (-10.16×10⁻⁴/yr) is lower than REA (-1.14×10⁻⁴/yr) and GIMMS (3.55×10⁻⁴/yr). The greening rate in VIP, GIM_4g and REA are 25.22% (with 41.44% significantly greening), 68.49% (with 38.32% significant greening) and 49.83% (with 56.83% significant greening), respectively. Large difference in these greenness trends were found,

and thus an integrated method is need.(Li et al., 2023) Shifts in vegetation phenology affect ecosystem structure (Kharouba et al., 2018; Yang and Rudolf, 2010), consequentially affecting biodiversity (Renner and Zohner, 2018), terrestrial carbon and water cycles (Piao et al., 2020), and the climate system (Green et al., 2017; Piao et al., 2020). The establishment of a comprehensive and reliable vegetation phenology dataset is therefore profoundly important. Our study demonstrates that an invaluable reliable vegetation phenology dataset can be obtained by applying the REA method, and that this dataset could be used for subsequent analyses, such as examining vegetation phenology dynamics and their impacts on the terrestrial carbon cycle and water balance, and providing climatic feedback for global vegetation dynamics modeling.

Data availability

The MCD12Q2 phenology dataset is available at https://lpdaac.usgs.gov/products/mcd12q2v061/(Friedl et al., 2022), the VIP phenology dataset is available at https://lpdaac.usgs.gov/products/vipphen_ndviv004/ (Didan and Barreto, 2016), the GIM_3g phenology dataset is available at http://data.globalecology.unh.edu/data/GIMMS_NDVI3g_Phenology/ (Wang et al., 2019), the GIM_4g phenology dataset is available at https://doi.org/10.5281/zenodo.11136967 (Chen and Fu, 2024), the camera-based phenology dataset is available at https://daac.ornl.gov/, http://www.sizenken.biodic.go.jp/, and http://www.pheno-eye.org/, the land use dataset is available at https://lpdaac.usgs.gov/products/mcd12q1v061/ (Friedl and Sulla-Menashe, 2022), and the REA phenology dataset is available at https://doi.org/10.5281/zenodo.11127281 (Cui and Fu, 2024).

Competing interests

The contact author declares that none of the authors has any competing interests.

Author contribution

YHF developed the preliminary conceptualization; YC performed the study, YC, YHF and YZ wrote the manuscript; YHF and YZ supervised the manuscript construction and revision; SC, YG, ML, ZJ participated in reviewing and editing the paper. All authors have read and approved the paper.

Acknowledgments

The work was supported by the National Funds for Distinguished Young Youths (Grant No. 42025101), the National Key Research and Development Program of China (Grant No. 2023YFF0805604), the Fundamental Research Funds for the Central Universities (2243300004), and the 111 Project (Grant No. B18006). We are grateful to the anonymous reviewers for their valuable suggestions that helped us strengthen the quality of our paper. We thank Liwen Bianji for editing the English text of a draft of this manuscript. Data used in this research were provided by the PhenoCam Network, which has been supported by

the National Science Foundation, the Long-Term Agroecosystem Research (LTAR) network which is supported by the United States Department of Agriculture (USDA), the U.S. Department of Energy, the U.S. Geological Survey, the Northeastern States Research Cooperative, and the USA National Phenology Network. We thank the PhenoCam Network collaborators, including site PIs and technicians, for publicly sharing the data that were used in this paper.

References

Badeck, F.-W., Bondeau, A., Böttcher, K., Doktor, D., Lucht, W., Schaber, J., and Sitch, S.: Responses of spring phenology to climate change, New Phytologist, 162, 295–309, https://doi.org/10.1111/j.1469-8137.2004.01059.x, 2004.

Blunden, J., Boyer, T., and Bartow-Gillies, E.: State of the Climate in 2022, Bulletin of the American Meteorological Society, 104, S107, https://doi.org/10.1175/2023BAMSStateoftheClimate.1, 2023.

Chen, S. and Fu, Y.: Vegetation phenology data based on GIMMS4g NDVI from 1982 to 2020 [data set], https://doi.org/10.5281/zenodo.11136967, 2024.

Chen, S., Fu, Y. H., Li, M., Jia, Z., Cui, Y., and Tang, J.: A new temperature–photoperiod coupled phenology module in LPJ-GUESS model v4. 1: optimizing estimation of terrestrial carbon and water processes, Geoscientific Model Development, 17, 2509–2523, https://doi.org/10.5194/gmd-17-2509-2024, 2024.

Chen, X., Wang, D., Chen, J., Wang, C., and Shen, M.: The mixed pixel effect in land surface phenology: A simulation study, Remote Sensing of Environment, 211, 338–344, https://doi.org/10.1016/j.rse.2018.04.030, 2018.

Cong, N., Piao, S., Chen, A., Wang, X., Lin, X., Chen, S., Han, S., Zhou, G., and Zhang, X.: Spring vegetation green-up date in China inferred from SPOT NDVI data: A multiple model analysis, Agricultural and Forest Meteorology, 165, 104–113, https://doi.org/10.1016/j.agrformet.2012.06.009, 2012.

Cui, Y. and Fu, Y.: A vegetation phenology dataset by integrating multiple sources using the Reliability Ensemble Averaging method [data set], https://doi.org/10.5281/zenodo.11127281, 2024.

Delbart, N., Beaubien, E., Kergoat, L., and Le Toan, T.: Comparing land surface phenology with leafing and flowering observations from the PlantWatch citizen network, Remote Sensing of Environment, 160, 273–280, https://doi.org/10.1016/j.rse.2015.01.012, 2015.

Didan, K. and Barreto, A.: NASA MEaSUREs Vegetation Index and Phenology (VIP) Phenology NDVI Yearly Global 0.05Deg CMG [data set], https://doi.org/10.5067/MEaSUREs/VIP/VIPPHEN_NDVI.004, 2016.

Didan, K., Barreto-Munoz, A., Miura, T., Tsend-Ayush, J., Zhang, X., Friedl, M., and Meyer, D.: Multi-Sensor Vegetation Index and Phenology Earth Science Data Records, 2018.

Ettinger, A. K., Chamberlain, C. J., Morales-Castilla, I., Buonaiuto, D. M., Flynn, D. F. B., Savas, T., Samaha, J. A., and Wolkovich, E. M.: Winter temperatures predominate in spring phenological responses to warming, Nature Climate Change, 10, 1137–1142, https://doi.org/10.1038/s41558-020-00917-3, 2020.

Fensholt, R. and Proud, S. R.: Evaluation of Earth Observation based global long term vegetation trends—Comparing

545   GIMMS and MODIS global NDVI time series, Remote sensing of Environment, 119, 131–147, https://doi.org/10.1016/j.rse.2011.12.015, 2012.

Friedl, M. and Sulla-Menashe, D.: MODIS/Terra+Aqua Land Cover Type Yearly L3 Global 500m SIN Grid V061 [data set], https://doi.org/10.5067/MODIS/MCD12Q1.061, 2022.

Friedl, M., Gray, J., and Sulla-Menashe, D.: MODIS/Terra+Aqua Land Cover Dynamics Yearly L3 Global 500m SIN
550   Grid V061 [data set], https://doi.org/10.5067/MODIS/MCD12Q2.061, 2022.

Fu, Y. H., Piao, S., Op de Beeck, M., Cong, N., Zhao, H., Zhang, Y., Menzel, A., and Janssens, I. A.: Recent spring phenology shifts in western C entral E urope based on multiscale observations, Global ecology and biogeography, 23, 1255–1263, https://doi.org/10.1111/geb.12210, 2014.

Gao, F., Masek, J., Schwaller, M., and Hall, F.: On the blending of the Landsat and MODIS surface reflectance: Predicting
555   daily Landsat surface reflectance, IEEE Transactions on Geoscience and Remote sensing, 44, 2207–2218, https://doi.org/10.1109/TGRS.2006.872081, 2006.

Geng, X., Fu, Y. H., Hao, F., Zhou, X., Zhang, X., Yin, G., Vitasse, Y., Piao, S., Niu, K., and De Boeck, H. J.: Climate warming increases spring phenological differences among temperate trees, Global Change Biology, 26, 5979–5987, https://doi.org/10.1111/gcb.15301, 2020.

560   Gevaert, C. M. and García-Haro, F. J.: A comparison of STARFM and an unmixing-based algorithm for Landsat and MODIS data fusion, Remote sensing of Environment, 156, 34–44, https://doi.org/10.1016/j.rse.2014.09.012, 2015.

Giorgi, F. and Mearns, L. O.: Calculation of Average, Uncertainty Range, and Reliability of Regional Climate Changes from AOGCM Simulations via the "Reliability Ensemble Averaging" (REA) Method, Journal of Climate, 15, 1141–1158, https://doi.org/10.1175/1520-0442(2002)015<1141:COAURA>2.0.CO;2, 2002.

565   Gray, J., Sulla-Menashe, D., and Friedl, M. A.: User guide to collection 6 modis land cover dynamics (mcd12q2) product, NASA EOSDIS Land Processes DAAC: Missoula, MT, USA, 6, 1–8, 2019.

Green, J. K., Konings, A. G., Alemohammad, S. H., Berry, J., Entekhabi, D., Kolassa, J., Lee, J.-E., and Gentine, P.: Regionally strong feedbacks between the atmosphere and terrestrial biosphere, Nature geoscience, 10, 410–414, https://doi.org/10.1038/ngeo2957, 2017.

570   Ide, R. and Oguma, H.: Use of digital cameras for phenological observations, Ecological Informatics, 5, 339–347, https://doi.org/10.1016/j.ecoinf.2010.07.002, 2010.

Inoue, T., Nagai, S., Saitoh, T. M., Muraoka, H., Nasahara, K. N., and Koizumi, H.: Detection of the different characteristics of year-to-year variation in foliage phenology among deciduous broad-leaved tree species by using daily continuous canopy surface images, Ecological Informatics, 22, 58–68, https://doi.org/10.1016/j.ecoinf.2014.05.009,
575   2014.

Jeong, S.-J., HO, C.-H., GIM, H.-J., and Brown, M. E.: Phenology shifts at start vs. end of growing season in temperate vegetation over the Northern Hemisphere for the period 1982–2008, Global change biology, 17, 2385–2399, https://doi.org/10.1111/j.1365-2486.2011.02397.x, 2011.

Kendall, M. G.: Rank correlation methods. 2nd impression, Charles Griffin and Company Ltd. London and High

580 Wycombe, 1975.

Kharouba, H. M., Ehrlén, J., Gelman, A., Bolmgren, K., Allen, J. M., Travers, S. E., and Wolkovich, E. M.: Global shifts in the phenological synchrony of species interactions over recent decades, Proceedings of the National Academy of Sciences, 115, 5211–5216, https://doi.org/10.1073/pnas.1714511115, 2018.

Li, M., Cao, S., Zhu, Z., Wang, Z., Myneni, R. B., and Piao, S.: Spatiotemporally consistent global dataset of the GIMMS
585 Normalized Difference Vegetation Index (PKU GIMMS NDVI) from 1982 to 2022 (V1.2) (V1.2) [data set], https://doi.org/10.5281/zenodo.8253971, 2023.

Liu, Q., Fu, Y. H., Zhu, Z., Liu, Y., Liu, Z., Huang, M., Janssens, I. A., and Piao, S.: Delayed autumn phenology in the Northern Hemisphere is related to change in both climate and spring phenology, Global change biology, 22, 3702–3711, 2016.

590 Lu, J., Wang, G., Chen, T., Li, S., Hagan, D. F. T., Kattel, G., Peng, J., Jiang, T., and Su, B.: A harmonized global land evaporation dataset from model-based products covering 1980–2017, Earth System Science Data, 13, 5879–5898, https://doi.org/10.5194/essd-13-5879-2021, 2021.

Ma, L., Zhou, Y., Chen, J., Cao, X., and Chen, X.: Estimation of Fractional Vegetation Cover in Semiarid Areas by Integrating Endmember Reflectance Purification Into Nonlinear Spectral Mixture Analysis, IEEE Geoscience and
595 Remote Sensing Letters, 12, 1175–1179, https://doi.org/10.1109/LGRS.2014.2385816, 2015.

Mao, P., Zhang, J., Li, M., Liu, Y., Wang, X., Yan, R., Shen, B., Zhang, X., Shen, J., and Zhu, X.: Spatial and temporal variations in fractional vegetation cover and its driving factors in the Hulun Lake region, Ecological Indicators, 135, 108490, https://doi.org/10.1016/j.ecolind.2021.108490, 2022.

Misra, G., Buras, A., and Menzel, A.: Effects of Different Methods on the Comparison between Land Surface and Ground
600 Phenology—A Methodological Case Study from South-Western Germany, Remote Sensing, 8, 753, https://doi.org/10.3390/rs8090753, 2016.

Moon, M., Richardson, A. D., and Friedl, M. A.: Multiscale assessment of land surface phenology from harmonized Landsat 8 and Sentinel-2, PlanetScope, and PhenoCam imagery, Remote Sensing of Environment, 266, 112716, https://doi.org/10.1016/j.rse.2021.112716, 2021.

605 Nasahara, K. N. and Nagai, S.: Review: Development of an in situ observation network for terrestrial ecological remote sensing: the Phenological Eyes Network (PEN), Ecological Research, 30, 211–223, https://doi.org/10.1007/s11284-014-1239-x, 2015.

Peng, D., Zhang, X., Wu, C., Huang, W., Gonsamo, A., Huete, A. R., Didan, K., Tan, B., Liu, X., and Zhang, B.: Intercomparison and evaluation of spring phenology products using National Phenology Network and AmeriFlux
610 observations in the contiguous United States, Agricultural and Forest Meteorology, 242, 33–46, https://doi.org/10.1016/j.agrformet.2017.04.009, 2017.

Peñuelas, J., Rutishauser, T., and Filella, I.: Phenology feedbacks on climate change, Science, 324, 887–888, https://doi.org/10.1126/science.1173004, 2009.

Piao, S., Fang, J., Zhou, L., Ciais, P., and Zhu, B.: Variations in satellite-derived phenology in China's temperate
615 vegetation, Global change biology, 12, 672–685, https://doi.org/10.1111/j.1365-2486.2006.01123.x, 2006.

Piao, S., Fang, J., Ciais, P., Peylin, P., Huang, Y., Sitch, S., and Wang, T.: The carbon balance of terrestrial ecosystems in China, Nature, 458, 1009–1013, https://doi.org/10.1038/nature07944, 2009.

620 Piao, S., Tan, J., Chen, A., Fu, Y. H., Ciais, P., Liu, Q., Janssens, I. A., Vicca, S., Zeng, Z., and Jeong, S.-J.: Leaf onset in the northern hemisphere triggered by daytime temperature, Nature communications, 6, 6911, https://doi.org/10.1038/ncomms7911, 2015.

Piao, S., Liu, Q., Chen, A., Janssens, I. A., Fu, Y., Dai, J., Liu, L., Lian, X. U., Shen, M., and Zhu, X.: Plant phenology and global climate change: Current progresses and challenges, Global change biology, 25, 1922–1940, https://doi.org/10.1111/gcb.14619, 2019a.

Piao, S., Liu, Q., Chen, A., Janssens, I. A., Fu, Y., Dai, J., Liu, L., Lian, X., Shen, M., and Zhu, X.: Plant phenology and
625 global climate change: Current progresses and challenges, Global Change Biology, 25, 1922–1940, https://doi.org/10.1111/gcb.14619, 2019b.

Piao, S., Wang, X., Park, T., Chen, C., Lian, X. U., He, Y., Bjerke, J. W., Chen, A., Ciais, P., and Tømmervik, H.: Characteristics, drivers and feedbacks of global greening, Nature Reviews Earth & Environment, 1, 14–27, https://doi.org/10.1038/s43017-019-0001-x, 2020.

630 Reed, B. C., Brown, J. F., VanderZee, D., Loveland, T. R., Merchant, J. W., and Ohlen, D. O.: Measuring phenological variability from satellite imagery, J Vegetation Science, 5, 703–714, https://doi.org/10.2307/3235884, 1994.

Renner, S. S. and Zohner, C. M.: Climate change and phenological mismatch in trophic interactions among plants, insects, and vertebrates, Annual review of ecology, evolution, and systematics, 49, 165–182, https://doi.org/10.1146/annurev-ecolsys-110617-062535, 2018.

635 Richardson, A. D., Anderson, R. S., Arain, M. A., Barr, A. G., Bohrer, G., Chen, G., Chen, J. M., Ciais, P., Davis, K. J., and Desai, A. R.: Terrestrial biosphere models need better representation of vegetation phenology: results from the N orth A merican C arbon P rogram S ite S ynthesis, Global Change Biology, 18, 566–584, https://doi.org/10.1111/j.1365-2486.2011.02562.x, 2012.

Richardson, A. D., Hufkens, K., Milliman, T., and Frolking, S.: Intercomparison of phenological transition dates derived
640 from the PhenoCam Dataset V1. 0 and MODIS satellite remote sensing, Scientific reports, 8, 5679, https://doi.org/10.1038/s41598-018-23804-6, 2018a.

Richardson, A. D., Hufkens, K., Milliman, T., Aubrecht, D. M., Chen, M., Gray, J. M., Johnston, M. R., Keenan, T. F., Klosterman, S. T., Kosmala, M., Melaas, E. K., Friedl, M. A., and Frolking, S.: Tracking vegetation phenology across diverse North American biomes using PhenoCam imagery, Sci Data, 5, 180028, https://doi.org/10.1038/sdata.2018.28,
645 2018b.

Ruan, Y., Ruan, B., Xin, Q., Liao, X., Jing, F., and Zhang, X.: phenoC++: An open-source tool for retrieving vegetation phenology from satellite remote sensing data, Frontiers in Environmental Science, 11, 215, https://doi.org/10.3389/fenvs.2023.1097249, 2023.

Seyednasrollah, B., Young, A. M., Hufkens, K., Milliman, T., Friedl, M. A., Frolking, S., and Richardson, A. D.: Tracking
650 vegetation phenology across diverse biomes using Version 2.0 of the PhenoCam Dataset, Scientific data, 6, 222, https://doi.org/10.1038/s41597-019-0229-9, 2019a.

Seyednasrollah, B., Young, A. M., Hufkens, K., Milliman, T., Friedl, M. A., Frolking, S., Richardson, A. D., Abraha, M., Allen, D. W., Apple, M., Arain, M. A., Baker, J., Baker, J. M., Baldocchi, D., Bernacchi, C. J., Bhattacharjee, J., Blanken, P., Bosch, D. D., Boughton, R., Boughton, E. H., Brown, R. F., Browning, D. M., Brunsell, N., Burns, S. P., Cavagna, M., Chu, H., Clark, P. E., Conrad, B. J., Cremonese, E., Debinski, D., Desai, A. R., Diaz-Delgado, R., Duchesne, L., Dunn, A. L., Eissenstat, D. M., El-Madany, T., Ellum, D. S. S., Ernest, S. M., Esposito, A., Fenstermaker, L., Flanagan, L. B., Forsythe, B., Gallagher, J., Gianelle, D., Griffis, T., Groffman, P., Gu, L., Guillemot, J., Halpin, M., Hanson, P. J., Hemming, D., Hove, A. A., Humphreys, E. R., Jaimes-Hernandez, A., Jaradat, A. A., Johnson, J., Keel, E., Kelly, V. R., Kirchner, J. W., Kirchner, P. B., Knapp, M., Krassovski, M., Langvall, O., Lanthier, G., Maire, G. l., Magliulo, E., Martin, T. A., McNeil, B., Meyer, G. A., Migliavacca, M., Mohanty, B. P., Moore, C. E., Mudd, R., Munger, J. W., Murrell, Z. E., Nesic, Z., Neufeld, H. S., O'Halloran, T. L., Oechel, W., Oishi, A. C., Oswald, W. W., Perkins, T. D., Reba, M. L., Rundquist, B., Runkle, B. R., Russell, E. S., Sadler, E. J., Saha, A., Saliendra, N. Z., Schmalbeck, L., Schwartz, M. D., Scott, R. L., Smith, E. M., Sonnentag, O., Stoy, P., Strachan, S., Suvocarev, K., Thom, J. E., Thomas, R. Q., et al.: Vegetation CollectionPhenoCam Dataset v2.0: Vegetation Phenology from Digital Camera Imagery, 2000-2018, https://doi.org/10.3334/ORNLDAAC/1674, 4 September 2019b.

Sisheber, B., Marshall, M., Mengistu, D., and Nelson, A.: Tracking crop phenology in a highly dynamic landscape with knowledge-based Landsat–MODIS data fusion, International journal of applied earth observation and geoinformation, 106, 102670, https://doi.org/10.1016/j.jag.2021.102670, 2022.

Sparks, T. H. and Carey, P. D.: The responses of species to climate over two centuries: an analysis of the Marsham phenological record, 1736-1947, Journal of Ecology, 321–329, https://doi.org/10.2307/2261570, 1995.

Sulla-Menashe, D. and Friedl, M. A.: User guide to collection 6 MODIS land cover (MCD12Q1 and MCD12C1) product, Usgs: Reston, Va, Usa, 1, 18, 2018.

Sun, J., Wang, X., Cao, Y., Li, H., and Jung, K.: Analysis of spatial and temporal evolution of hydrological and meteorological elements in Nenjiang River basin, China, Theoretical and applied climatology, 137, 941–961, https://doi.org/10.1007/s00704-018-2641-z, 2019.

Tang, J., Körner, C., Muraoka, H., Piao, S., Shen, M., Thackeray, S. J., and Yang, X.: Emerging opportunities and challenges in phenology: a review, Ecosphere, 7, e01436, https://doi.org/10.1002/ecs2.1436, 2016.

Trishchenko, A. P., Cihlar, J., and Li, Z.: Effects of spectral response function on surface reflectance and NDVI measured with moderate resolution satellite sensors, Remote Sensing of Environment, 81, 1–18, https://doi.org/10.1016/S0034-4257(01)00328-5, 2002.

Walker, J. J., De Beurs, K. M., Wynne, R. H., and Gao, F.: Evaluation of Landsat and MODIS data fusion products for analysis of dryland forest phenology, Remote Sensing of Environment, 117, 381–393, 2012.

Wang, X., Piao, S., Xu, X., Ciais, P., MacBean, N., Myneni, R. B., and Li, L.: Has the advancing onset of spring vegetation green-up slowed down or changed abruptly over the last three decades?, Global Ecology and Biogeography, 24, 621–631, https://doi.org/10.1111/geb.12289, 2015.

Wang, X., Xiao, J., Li, X., Cheng, G., Ma, M., Zhu, G., Altaf Arain, M., Andrew Black, T., and Jassal, R. S.: No trends in spring and autumn phenology during the global warming hiatus, Nat Commun, 10, 2389, https://doi.org/10.1038/s41467-019-10235-8, 2019.

White, M. A., de Beurs, K. M., Didan, K., Inouye, D. W., Richardson, A. D., Jensen, O. P., O'keefe, J., Zhang, G.,

690 Nemani, R. R., and van Leeuwen, W. J.: Intercomparison, interpretation, and assessment of spring phenology in North America estimated from remote sensing for 1982–2006, Global change biology, 15, 2335–2359, https://doi.org/10.1111/j.1365-2486.2009.01910.x, 2009.

Wu, W., Sun, Y., Xiao, K., and Xin, Q.: Development of a global annual land surface phenology dataset for 1982–2018 from the AVHRR data by implementing multiple phenology retrieving methods, International Journal of Applied Earth
695 Observation and Geoinformation, 103, 102487, https://doi.org/10.1016/j.jag.2021.102487, 2021.

Xu, Y., Gao, X., and Giorgi, F.: Upgrades to the reliability ensemble averaging method for producing probabilistic climate-change projections, Climate Research, 41, 61–81, https://doi.org/10.3354/cr00835, 2010.

Yang, L. H. and Rudolf, V. H. W.: Phenology, ontogeny and the effects of climate change on the timing of species interactions, Ecology letters, 13, 1–10, https://doi.org/10.1111/j.1461-0248.2009.01402.x, 2010.

700 Zeng, L., Wardlow, B. D., Xiang, D., Hu, S., and Li, D.: A review of vegetation phenological metrics extraction using time-series, multispectral satellite data, Remote Sensing of Environment, 237, 111511, https://doi.org/10.1016/j.rse.2019.111511, 2020.

Zhang, H., Chuine, I., Regnier, P., Ciais, P., and Yuan, W.: Deciphering the multiple effects of climate warming on the temporal shift of leaf unfolding, Nature Climate Change, 12, 193–199, https://doi.org/10.1038/s41558-021-01261-w,
705 2022.

Zhang, J., Zhao, J., Wang, Y., Zhang, H., Zhang, Z., and Guo, X.: Comparison of land surface phenology in the Northern Hemisphere based on AVHRR GIMMS3g and MODIS datasets, ISPRS Journal of Photogrammetry and Remote Sensing, 169, 1–16, 2020.

Zhou, X., Geng, X., Yin, G., Hänninen, H., Hao, F., Zhang, X., and Fu, Y. H.: Legacy effect of spring phenology on
710 vegetation growth in temperate China, Agricultural and Forest Meteorology, 281, 107845, https://doi.org/10.1016/j.agrformet.2019.107845, 2020.

Zhou, Y.: Understanding urban plant phenology for sustainable cities and planet, Nature Climate Change, 12, 302–304, https://doi.org/10.1038/s41558-022-01331-7, 2022.

Zhou, Y. and Liu, J.: Spatio-temporal Analysis of Vegetation Phenology with Multiple Methods over the Tibetan Plateau
715 based on MODIS NDVI Data, Remote Sensing Technology and Application, 33, 486–498, https://doi.org/10.11873/j.issn.1004-0323.2018.3.0486, 2018.

Zhu, X., Chen, J., Gao, F., Chen, X., and Masek, J. G.: An enhanced spatial and temporal adaptive reflectance fusion model for complex heterogeneous regions, Remote Sensing of Environment, 114, 2610–2623, https://doi.org/10.1016/j.rse.2010.05.032, 2010.